



1 **Modeling demographic-driven vegetation dynamics and ecosystem biogeochemical cycling**
2 **in NASA GISS's Earth system model (ModelE-BiomeE v.1.0)**

3

4 Ensheng Weng^{1,2}, Igor Aleinov^{1,2}, Ram Singh^{1,2}, Michael J. Puma^{1,2}, Sonali S. McDermid³,
5 Nancy Y. Kiang², Maxwell Kelley², Kevin Wilcox⁴, Ray Dybzinski⁵, Caroline E. Farrior⁶,
6 Stephen W. Pacala⁷, Benjamin I. Cook²

7

8 ¹Center for Climate Systems Research, Columbia University, New York, NY 10025, USA

9 ²NASA Goddard Institute for Space Studies, 2880 Broadway, New York, NY 10025, USA

10 ³Department of Environmental Studies, New York University, New York, NY 10003, USA

11 ⁴Department of Ecosystem Science and Management, University of Wyoming, Laramie, WY
12 82071, USA

13 ⁵Institute of Environmental Sustainability, Loyola University Chicago, Chicago, IL 60660, USA

14 ⁶Department of Integrative Biology, University of Texas at Austin, Austin, TX 78712, USA

15 ⁷Department of Ecology & Evolutionary Biology, Princeton University, Princeton, NJ 08544 ,
16 USA

17

18 **Corresponding author:** Ensheng Weng (wengensheng@gmail.com; phone: 212-678-5585)

19

20

21

22



23 **Abstract:** We developed a new demographic vegetation model, BiomeE, to improve the
24 representation of vegetation demographic dynamics and ecosystem biogeochemical cycles in the
25 NASA Goddard Institute of Space Studies' ModelE Earth system model. This model includes the
26 processes of plant growth, mortality, reproduction, vegetation structural dynamics, and soil
27 carbon and nitrogen storage and transformations. The model combines the plant physiological
28 processes of ModelE's original vegetation model, Ent, with minor adaptations to fit the new
29 allometry and vegetation structure with the plant demographic and ecosystem nitrogen processes
30 represented from Geophysical Fluid Dynamics Laboratory (GFDL)'s LM3-PPA. For global
31 applications, we added a new set of plant functional types to represent global vegetation
32 functional diversity, including trees, shrubs, and grasses, and a new phenology model to deal
33 with seasonal changes in temperature and soil water availability. Competition for light and soil
34 resources is individual based, which makes the modeling of transient compositional changes and
35 vegetation succession possible. BiomeE will allow ModelE to simulate long-term biogeophysical
36 and biogeochemical feedbacks between the climate system and land ecosystems. BiomeE
37 simulates, with fidelity comparable to other models, the dynamics of vegetation and soil
38 biogeochemistry, including leaf area index, vegetation structure (e.g., height, tree density, size
39 distribution, crown organization), and ecosystem carbon and nitrogen storage and fluxes.
40 Further, BiomeE will also allow for the simulations of transient vegetation dynamics and eco-
41 evolutionary optimal community assemblage in response to past and future climate changes by
42 incorporating core ecological processes, including demography, competition, and community
43 assembly.

44 **Key words:** Biogeochemical cycles, Eco-evolutionary optimality, Ecosystem modeling, Plant
45 traits, Vegetation dynamics



1 **1 Introduction**

2 Terrestrial ecosystems play a critical role in the climate system by regulating exchanges of
3 energy, moisture, and carbon dioxide between the land surface and the atmosphere (Sellers,
4 1997; Pielke et al., 1998; Meir et al., 2006). In turn, climate change has significantly affected
5 vegetation photosynthesis, water use efficiency, mortality, regeneration, and structure through
6 gradual changes in temperature and atmospheric [CO₂] together with shifts in climate extremes
7 (Brando et al., 2019; McDowell et al., 2020; Keenan et al., 2013; Huang et al., 2015). These
8 responses have triggered vegetation structural and compositional shifts. For example, global
9 forest mortality has increased in recent years (Allen et al., 2010; Anderegg et al., 2012), tree
10 sizes have decreased (Zhou et al., 2014; McDowell et al., 2020), and species composition has
11 shifted to more opportunistic species (Clark et al., 2016; Brodribb et al., 2020). The shifts in
12 vegetation function, composition, and structure can change the boundary conditions of the land
13 surface and affect the climate system (Nobre et al., 1991; Avissar and Werth, 2005; Garcia et al.,
14 2016; Green et al., 2017; Zeng et al., 2017). Realistically simulation of these processes is
15 therefore critical for Earth system models (ESMs).

16 The vegetation dynamics in ESMs are usually simulated using dynamic global vegetation
17 models (DGVMs) (Prentice et al., 2007), most of which are simplified in their representation of
18 ecological processes. The core assumptions of many vegetation models are a big-leaf canopy,
19 vegetation represented by only a few plant functional types (PFTs), single cohort-based
20 vegetation dynamics (“single-cohort” assumption, where the vegetation community at a land unit
21 are simulated as a collection of identical trees), lumped-pool-based biogeochemical cycles and
22 first order decay of soil organic matter. The competition of plant individuals and vegetation types
23 is approximately simulated as a function of productivity or Lotka-Volterra equations to predict



24 fractional PFT coverage (e.g., SDVGM, HYBRID, TRIFFID) (Friend et al., 1997; Woodward et
25 al., 1998; Sitch et al., 2003). These simplifying assumptions make it possible to simulate the
26 complex interactions of biological and ecological processes at the global scale.

27 These models are generally successful in reproducing land surface carbon, energy, and
28 water fluxes after extensive tuning against data from sites, observational networks, and satellite
29 remote sensing. However, the uncertainty of model predictions is high, and predictions can
30 diverge substantially across different models (Friedlingstein et al., 2014; Arora et al., 2020).
31 Lack of functional diversity and community assembly processes is one of the key issues in the
32 vegetation modeling of ESMs, which makes the models unable to predict transient dynamics of
33 vegetation composition and structure. A more mechanistic design that uses the fundamental
34 principles of ecology to simulate the emergent properties of ecosystems for predicting ecosystem
35 dynamics may therefore be necessary (Weng et al., 2017; Scheiter et al., 2013).

36 To this end, extensive efforts have been made to improve the representation of transient
37 vegetation dynamics based on ecological theories and conceptual models. Two pivotal advances
38 have been made in ecological vegetation modeling: 1) Demographic processes and trait-based
39 representation of processes have been developed to improve the representation of functional
40 diversity and size structure (Fisher et al., 2015; Weng et al., 2015; Pavlick et al., 2013) and 2)
41 eco-evolutionary optimal and game theoretical approaches have been proposed to predict the
42 flexibility of parameters and processes (McNickle et al., 2016; Weng et al., 2017). These
43 concepts are mainly applied in modeling photosynthesis (Wang et al., 2017; Prentice et al.,
44 2014), allocation (Farrion et al., 2013; Dybzinski et al., 2015), and evolutionarily stable strategy
45 (ESS) of plant traits (Falster et al., 2017; Weng et al., 2017). These ideas for incorporating
46 ecological and evolutionary principles into ESMs have been summarized in several recent review



47 papers (Harrison et al., 2021; Franklin et al., 2020; Kyker-Snowman et al., 2022). Microbial
48 processes have also been added to the decomposition models for soil organic matter (Sulman et
49 al., 2019; Wieder et al., 2014; Lu and Hedin, 2019).

50 There are still major challenges to integrating these more sophisticated ecological modeling
51 approaches into the complex land models of ESMs, where the explicit simulations of energy,
52 water, and carbon fluxes at high frequencies are required for interacting with the atmosphere and
53 climate system. The details of vegetation dynamics, including the key functions from leaf
54 photosynthesis, respiration, biogeochemical fluxes between pools, demographic processes,
55 community assembly, vegetation structure, and competition output, must be well-organized
56 hierarchically and computed efficiently (Fisher and Koven, 2020; Franklin et al., 2020).
57 Representing these processes in ESMs, however, can complicate model structure and behavior,
58 especially for the interaction between physiology and vegetation composition, and cause large
59 increases in the computational burden. Thus, the implementation of detailed vegetation
60 demographic processes and size categories into ESMs would benefit from more parsimonious
61 approaches, such as is the case for the Robust Ecosystem Demography model (Argles et al.,
62 2020).

63 Including highly complex processes does not necessarily increase model predictive skills
64 (Famiglietti et al., 2021; Forster, 2017; Hourdin et al., 2017). On the contrary, it may greatly
65 obscure model transparency and increase uncertainty, and positive feedbacks in these processes
66 may result in large and unanticipated shifts of vegetation states. Any small differences in model
67 setting or even parameter differences can result in distinct predictions, especially in vegetation
68 structure, which is supposed to be predicted by these types of models. These processes make
69 demographic vegetation models often unreliable when compared to the well-tuned “single-



70 cohort” vegetation models that simplify the reproduction and mortality as growth and turnover of
71 continuous biomass pools. Additionally, the legacy of land models and the technical
72 requirements of reversibility in model development mean developers must often build their new
73 functions on top of their previous assumptions and model structure (Fisher and Koven, 2020),
74 adding up to multiple adjustments on top of previous assumptions and making the model
75 untraceable.

76 To explicitly model the transient dynamics of ecosystems in ESMs while preserving model
77 traceability, we need clear assumptions, detailed physical processes, and traceable model
78 structure. For the best chance of accurate predictions outside of the model's testing data, model
79 processes should be based on the fundamental biological and ecological principles to predict
80 ecosystem emergent properties, instead of fitting the emergent patterns directly as many models
81 do currently. To achieve this, we need to properly represent the tradeoffs of plant traits, balance
82 the complexity of the model structure and priority for the processes that are required by the
83 general circulation model (GCM), and also make model assumptions transparent and processes
84 robust. These requirements make it difficult to fully implement the modeling approaches that are
85 well-developed in the ecological modeling community.

86 The NASA Goddard Institute for Space Studies’ Earth system model, ModelE, has a land
87 model for representing land surface hydrology (TerraE) (Rosenzweig and Abramopoulos, 1997;
88 Schmidt et al., 2014) and a vegetation biophysics scheme (from the Ent Terrestrial Biosphere
89 Model)(Ito *et al.* 2020; Kelley *et al.* 2020; Schmidt *et al.* 2014), with fixed vegetation traits (e.g.,
90 leaf mass per area, C:N ratio), fixed biomass, canopy height, and plant density, and seasonal leaf
91 area index prescribed from a satellite-derived data set (Ito et al., 2020). The Ent TBM calculates
92 canopy radiative transfer (Friend & Kiang 2005), canopy albedo, canopy conductance,



93 photosynthesis, autotrophic respiration, and some phenological behaviors of leaf biophysics
94 (Kim et al., 2015). The carbon allocation scheme of Kim et al. (2015) is used in ModelE with
95 prescribed canopy structure and LAI, routing the carbon that would otherwise be allocated to
96 plant tissues via growth instead directly as litter into soil carbon pools, thus conserving carbon
97 for fully coupled carbon cycle simulations, but resulting possibly in imbalanced plant carbon
98 reserve pools where the prescribed canopy structure is not in equilibrium with the simulated
99 climate (Ito et al., 2020).

100 This paper describes a parsimonious vegetation demographic and soil organic
101 decomposition model that can be incorporated into the GISS ModelE ESM. Our goal is to
102 develop a parsimonious, transparent model that 1) allows ModelE to simulate the ecological
103 dynamics of terrestrial ecosystems and vegetation at the global scale and 2) sets up a modeling
104 framework for solving some of the major challenges for incorporating important ecological
105 mechanisms into ESMs. For (1), we have incorporated core ecosystem processes, including plant
106 growth, demography, community assembly, and ecosystem carbon and nitrogen cycles. For (2),
107 we have developed PFTs that are plant trait-based and a competition scheme that is individual-
108 based. In this paper, we describe this model in detail, and evaluate its performance compared to
109 both observations and other state-of-the-art DGVMs.

110

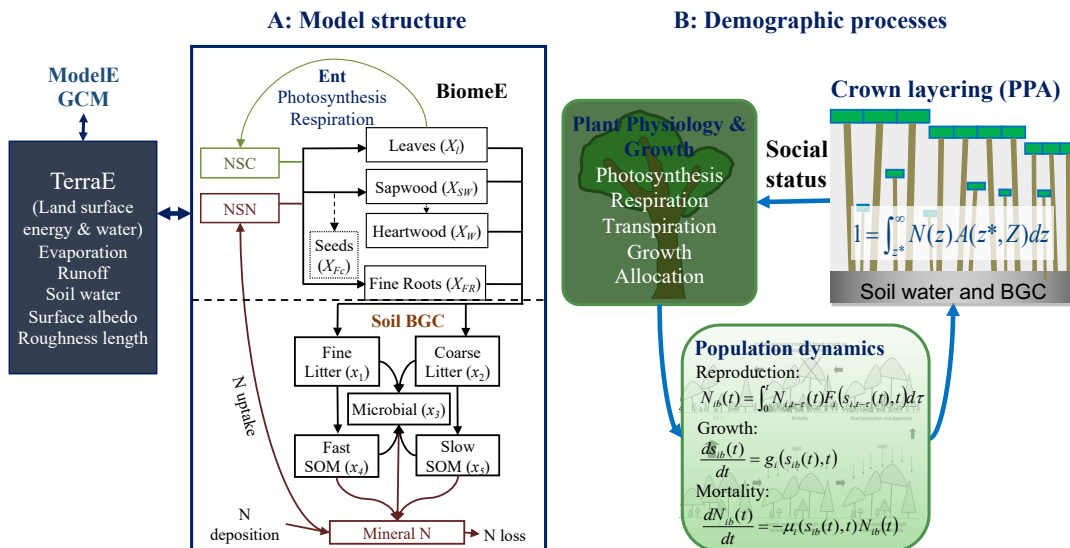
111 **2 Model Description**

112 **2.1 BiomeE Structure and Overview**

113 BiomeE is a standalone simulator derived from the LM3-PPA (Weng et al., 2015). It is a
114 demographic vegetation model that simulates plant physiology, vegetation demography, adaptive
115 dynamics (eco-evolutionary adaptation), and ecosystem carbon, nitrogen, and water cycles (Fig.



116 1) (Weng et al., 2017, 2019). In this model, a PFT is defined by a set of combined plant traits
 117 with their values sampled from the observed ranges to represent a specific plant type. The
 118 individual is the basic unit to carry out physiological and demographic activities, e.g.,
 119 photosynthesis, respiration, growth, reproduction, mortality, and competition with other
 120 individuals. Individual plants are categorized into cohorts and arranged in different vertical
 121 canopy layers according to their height and crown area following the rules of the Perfect
 122 Plasticity Approximation model (PPA, Strigul et al., 2008). Sunlight is partitioned into canopy
 123 crown layers according to Beer's law. With the PPA model, a key parameter for light
 124 competition, the height of canopy closure (i.e., critical height, H^*), is defined; all the plants
 125 above this context-dependent height get full sunlight and all trees below this height are shaded
 126 by the upper layer trees.



127
 128 **Figure 1 Schematic diagram of the coupling of BiomeE into ModelE**
 129 Panel A shows the structure of carbon and nitrogen pools and fluxes, and the interactions of
 130 BiomeE with TerraE, the land surface model in ModelE. The lines are the flows of carbon
 131 (green), nitrogen (brown), and coupled carbon and nitrogen (black). The green box is for carbon
 132 only. The brown boxes are N pools. The black boxes are for both carbon and nitrogen pools. The



133 C:N ratios of leaves, wood, fine roots, and microbes are fixed and those of liters and SOM pools
134 are dynamic with input and output. Panel b shows the demographic processes of BiomeE and the
135 key processes of population dynamics.

136

137 The demographic processes generate and remove cohorts and change the size and density of
138 plant individuals in the cohorts. With explicit description of cohort size, organization, and
139 composition during a model run, the model simulates competition for light and soil resources,
140 community assembly and vegetation structural dynamics. These processes are hierarchically
141 organized in this model and run at various time steps: half-hourly or hourly for plant physiology
142 and soil organic matter decomposition, daily for growth and phenology, and yearly for
143 demography.

144 We coupled the standalone BiomeE into ModelE's land model for simulating global
145 dynamics of vegetation and biogeochemical cycles and their feedback to the climate systems. For
146 extrapolating this model to the global scale, we designed a new set of PFTs to represent the
147 functional diversity of global vegetation and a new phenological scheme to deal with
148 environmental seasonality and water conditions across the world. Leaf photosynthesis processes
149 are from ModelE's existing vegetation model, Ent (Kim et al. 2015), for calculating carbon
150 budget that drives vegetation dynamics. Plant growth and demographic processes and the soil
151 organic matter decomposition and nitrogen cycle processes are from BiomeE (Fig. 1). The land
152 surface energy and water fluxes are calculated by TerraE with land surface characteristics jointly
153 defined by the vegetation model.

154 **Plant functional types**

155 We defined 9 PFTs in our test runs to represent global vegetation functional diversity
156 (Table 1) according to their life form (tree, shrub, and grass), photosynthesis (C₃ and C₄), and



157 leaf phenology (evergreen and deciduous). A set of continuous plant traits are used to define the
 158 distinctive plant types, because we plan to simulate plant emergent behavior based on their
 159 fundamental properties with this model in the future. For example, life forms are along the
 160 continuums characterized by wood density (woody vs. herbaceous), height growth coefficient
 161 (tree vs. shrub), and leaf mass per unit area (LMA, for evergreen vs. deciduous). Deciduousness
 162 is defined by cold resistance (evergreen vs. cold deciduous), and drought resistance (evergreen
 163 vs. drought deciduous), and the photosynthesis pathway is predefined as C₃ or C₄. Grasses are
 164 simulated as tree seedlings with all stems senescent along with leaves at the end of a growing
 165 season. The individuals are reset back to initial size each year and the population density is also
 166 reset using the total biomass of current cohort and predefined initial size of grasses.

167 **Table 1 Plant functional types used in BiomeE**

Plant functional types	V_{cmax}	LMA (kg C m ⁻²)	ρ_{W} (kg C m ⁻³)	α_{H}	$T_{0,\text{c}}$	$\beta_{0,\text{D}}$	PS pathway
1. Tropical evergreen broadleaf	18	0.07	360	30	15	0	C ₃
2. Temperate/boreal evergreen needleleaf	18	0.14	300	30	-80	0	C ₃
3. Temperate/boreal deciduous broadleaf	22	0.025	350	30	15	0	C ₃
4. Tropical drought deciduous broadleaf	20	0.03	250	30	15	0.2	C ₃
5. Boreal deciduous needleleaf	20	0.03	300	30	15	0.0	C ₃
6. Cold shrub	18	0.025	360	20	15	0.1	C ₃
7. Arid shrub	18	0.03	360	20	15	0.1	C ₃
8. C ₃ grass	20	0.025	90*	10	5	0.2	C ₃
9. C ₄ grass	15	0.025	90*	10	5	0.2	C ₄

168 LMA: leaf mass per unit area, ρ_{W} : wood density, α_{H} : Height coefficient, $T_{0,\text{c}}$: Critical
 169 temperature for phenology offset, $\beta_{0,\text{D}}$: critical soil moisture index for the offset of phenology,
 170 PS: photosynthesis pathway, E: evergreen, C: cold-deciduous, D: drought-deciduous. *Grass
 171 stem density is calculated as tissue biomass divided by stem volume. The tissue density of
 172 grass's stems is as high as wood.



173

174 All PFTs go through the same set of plant physiological and demographical processes in
175 the model and derive different emergent properties due to the differences in parameters, rather
176 than differences in processes (except C₃ and C₄). With these different strategies, they have their
177 advantages and risks in different environments. An advantage of this continuous parameter
178 design is that one PFT can switch to another by changing its parameters (except C₃ and C₄
179 photosynthesis pathways). This opens the way for eco-evolutionary and ecological community
180 assembly simulation to explore the competitively optimal plant traits as environments change.

181 **Phenology**

182 Phenology types are defined by two parameters, a critical low temperature and a critical soil
183 moisture index, that are used to trigger leaf fall. These two parameters define 4 phenological
184 types for all the 9 PFTs: evergreen, drought-deciduous, cold-deciduous, and drought-cold-
185 deciduous. Evergreen PFTs have high resistances to cold (i.e., very low critical temperature) and
186 drought (very low soil drought). Cold and drought deciduous PFTs have low critical temperature
187 and soil drought index, respectively.

188 For the cold-deciduous PFTs (3 and 5), we used the growing degree days above 5 °C
189 (GDD_5) to control the timing of phenological onset and a critical low temperature (T_m) to control
190 the offset. GDD_5 is calculated from the days that temperature starts to increase from the coldest
191 days in the non-growing season. The critical value of GDD that the plants require for growth
192 (GDD_c) is defined as a function of chilling days in the non-growing season (Prentice et al.,
193 1992):

$$GDD_c = a_0 + d \cdot e^{-b \cdot N_{CD}}, \quad (1)$$



194 where, N_{CD} is the days of the cold period in nongrowing season before bud burst, a_0 is the
195 minimum GDD_c (50) when the cold period is sufficiently long, d is the maximum addition of
196 GDD_c (800) when there is no cold period (i.e., $N_{CD}=0$), b is a shape coefficient (0.025). These
197 parameters are tunable and should change with acclimate to new climates.

198 The running mean temperature that represents the mean temperatures over a short period of time
199 is calculated as:

$$\begin{cases} T_m(i) = T_d(i), & \text{when } i = 1 \\ T_m(i) = 0.8T_m(i-1) + 0.2T_d(i), & \text{when } i \geq 2 \end{cases} \quad (2)$$

200 We used an index of cold condition (accumulative low temperature, ALT) to make sure the low
201 temperature signal is persistent and differentiates the signal of the seasonal temperature changes
202 and the stochastic low temperature stresses in growing seasons. The critical temperature for
203 triggering leaf senescence (T_c) is calculated as a function of the number of growing days (N_{GD}).

$$T_c = T_{0,c} - s \cdot e^{-c \cdot (\max(0, N_{GD} - L0))}, \quad (3)$$

204 where, $T_{0,c}$ is the highest critical temperature when N_{GD} is sufficiently long, s is the range that a
205 critical temperature can change, c is a shape parameter, $L0$ defines the lowest critical temperature
206 ($T_{0,c} - s$) when N_{GD} is smaller than $L0$. The rationale in this equation is that when a growing
207 period is not long enough, plants need a lower T_c to trigger leaf fall so that they can have a
208 growing season that is not too short. This setting is based on the thermal adaptation analysis of
209 Yuan et al. (2011).

210 For the drought deciduous PFTs (tropical drought deciduous broadleaf, arid shrub, C₄
211 grass), we used a soil moisture index (s_D) to initiate and terminate a growing season.



$$s_D = \sum_{i=1}^n \text{Min} \left(1.0, \max \left(\frac{\theta_i - \theta_{WP,i}}{\theta_{HC,i} - \theta_{WP,i}}, 0.0 \right) \right), \quad (4)$$

212 where i is the soil layer in root zone, θ is soil water content (vol/vol), θ_{WP} is wilting point, and
213 θ_{HC} is soil water holding capacity. The critical soil moisture (θ^*) that triggers leaf fall is defined
214 as a PFT-specific parameter with evergreen PFTs having low θ^* .

215 Plant demography and biogeochemical cycles

216 Allometry and Plant architecture

217 The allometry of woody PFTs follows the equations used in LM3-PPA (Weng et al., 2015;
218 Farrior et al., 2013). Plant allometry is described by the following equations:

$$\begin{cases} A_C = \alpha_C D^{\theta_C} \\ Z = \alpha_Z D^{\theta_Z} \\ S = 0.25\pi\rho\Lambda\alpha_H D^{2+\theta_H} \\ A_L^* = l_{max} A_C \\ A_{FR}^* = \varphi_{RL} l_{max} A_C \end{cases} \quad (5)$$

219 where D is tree diameter; A_C is crown area; Z is tree height; S is structural biomass; α_C , α_Z , θ_C ,
220 θ_Z , are the allometry parameters for crown area and tree height, respectively; π is ratio of a
221 circle's circumference to its diameter; ρ is wood density (kg C m^{-3}); Λ is the taper factor from a
222 cylinder to a tree with the same D ; A_L^* and A_{FR}^* are the surface area of leaves and fine roots,
223 respectively; φ_{RL} is the area ratio of leaves to roots. l_{max} is potential leaf area per unit crown area
224 (i.e., potential crown LAI), defined as a function of plant height (Z):

$$l_{max}(Z) = L_{max,0}(Z + h_0)/(Z + H_0), \quad (6)$$



225 where $L_{\max,0}$ is the maximum crown LAI when a tree is sufficiently tall, H is tree height, h_0 is a
226 small number that makes a minimum $l_{\max}(L_{\max,0}(h_0/H_0))$ when tree height is close to zero, and
227 H_0 is a curvature parameter.

228 **Plant growth and allocation of carbon and nitrogen to plant tissues**

229 BiomeE has an optimal allocation scheme for allocating assimilated carbon to different tissues
230 when nitrogen supply is limited (Weng et al., 2019). This allocation scheme prioritizes the
231 allocation to leaves and fine roots, while maintaining a minimum growth rate of stems and
232 keeping the constant area ratio of fine roots to leaves during the lifetime of a plant. According to
233 these rules, the average allocations of carbon and nitrogen to leaves, fine roots, and wood over a
234 growing season are governed by the targets for the leaf area per unit crown area (i.e., crown leaf
235 area index, l^*) and fine root area per unit leaf area (ϕ_{RL}). We assume the allocation between
236 structural (e.g., stems) and functional (e.g., leaves and fine roots) tissues is that which is optimal
237 for a given nitrogen availability, optimizing the use of carbon gain and light competition.

238 Wood tissue growth (G_W) drives the growth of tree diameter, height, and crown area and thus
239 increases the targets of leaves and fine roots. By differentiating the stem biomass allometry in
240 Eq. 5 with respect to time, using the fact that dS/dt equals the carbon allocated for wood growth
241 (G_W), we have the diameter growth:

$$\frac{dD}{dt} = \frac{G_W}{0.25\pi\Lambda\rho_w\alpha_z(2+\theta_z)D^{1+\theta_z}} \quad (7)$$

242 This equation transforms the carbon gain from photosynthesis to the diameter growth that results
243 from wood allocation and allometry (Eq 5). With an updated tree diameter, we then calculate the
244 new tree height and crown area using allometry equations and targets of leaf and fine root
245 biomass (Eq. 5).



246 **Reproduction and Mortality**

247 At a yearly time-step, the cumulative carbon and nitrogen allocated for reproducing by a canopy
248 cohort over the growing season length, T , is converted to seedlings according to the initial plant
249 biomass (S_0) and germination and establishment probabilities (p_g and p_e , respectively).

250 Generally, the population dynamics can be described by a variant of the von Foerster equation
251 (von Foerster, 1959):

$$N(S_0, t) = \frac{p_g p_e}{S_0} \int_0^T N(\tau) G_F(\tau) d\tau \quad (8)$$
$$\frac{dN(s,t)}{dt} = -\mu(s, t)N(s, t).$$

252 where $N(S_0, t)$ is the spatial density of newly generated seedlings, $N(\tau)$ is the spatial density of
253 this cohort of trees at time τ , G_F is the carbon allocation to seeds, and μ is PFT-specific mortality
254 parameter. Each PFT has a canopy-layer-specific background mortality rate that is assigned from
255 the literature. These background rates are assumed to be size-independent for the canopy layer
256 trees, but size-dependent for understory trees. Many factors affect tree mortality, such as light,
257 size, competition crown damage, hydraulic failure, trunk damage etc. (Zuleta et al., 2022; Lu et
258 al., 2021). These factors result in a “U-shaped” general mortality curve. We assume the
259 background mortality rate is represented as a function of vertical position (light fraction) and tree
260 size

$$\mu(s, t) = \mu_0(1 + f_L f_s) f_D \quad (9)$$

261 where $f_L = \sqrt{L - 1}$, $f_s = A_{SD} e^{-B_{SD} D}$, and $f_D = m_s \frac{e^{A_D(D-D_0)}}{1 + e^{A_D(D-D_0)}}$. L is the layer this plant is in
262 ($L=1$ for the canopy layer and 2 for the second, and so on), A_{SD} is the maximum multiplier of
263 mortality rate for the seedlings in the understory layers, B_{SD} is the rate of mortality decreasing as



264 tree diameter (D) increases, m_s is the maximum multiplier of mortality rate for large-sized trees,
265 D_0 is the diameter at which the mortality rate increases by $m_s/2$, and A_D is a shape parameter
266 (i.e., the sensitivity to tree diameter).

267 **Crown self-organization and layering**

268 Tree crowns are arranged into different vertical canopy layers according to tree height and
269 crown area if their total crown area is greater than the land area following the rules of the PPA
270 model (Strigul et al., 2008). In PPA, individual tree height is defined as the height at the top of
271 the crown, and all leaves of a given cohort are assumed to belong to a single canopy layer. The
272 height of canopy closure for the top layer is referred to as critical height (Z^* , the height of the
273 shortest tree in the layer) and is defined implicitly by the following equation:

$$k(1 - \eta) = \sum_i \int_{Z^*}^{\infty} N_i(Z, t) A_{CR,i}(Z^*, Z) dZ \quad (10)$$

274 where $N_i(Z, t)$ is the density of PFT i trees of height Z per unit ground area; $A_{CR,i}(Z^*, Z)$ is the
275 crown area of an individual PFT i tree of height Z ; and η is the proportion of each canopy layer
276 that remains open on average due to wind and imperfect spacing between individual tree crowns.

277 The top layer includes the tallest cohorts of trees whose collective crown area sums to $1 - \eta$
278 times the ground area; lower layers are similarly defined. Trees within the same layer do not
279 shade each other, but there is self-shading among the leaves within individual crowns. Cohorts in
280 a sub-canopy layer are shaded by the leaves of all taller canopy layers. In each canopy layer, all
281 cohorts are assumed to have the same incident radiation on the top of their crowns. Note, the gap
282 fraction η is necessary to allow additional light penetration through each canopy layer for the
283 persistence of understory trees in monoculture forests in which the upper layer crowns build a
284 physiologically-optimal number of leaf layers (Farrior et al., 2013). The grasses only form one



285 layer. Those individuals who cannot stay in that layer because of limited space will be killed
286 (i.e., when the total grass crown area is larger than the land area).

287 **Ecosystem carbon and nitrogen biogeochemical cycles**

288 Ecosystem biogeochemical cycles (carbon and nitrogen in this model) are driven by plant and
289 microbial demographic processes. There are seven pools in each plant: leaves, fine roots,
290 sapwood, heartwood, fecundity (seeds), and non-structural carbohydrates and nitrogen (NSC and
291 NSN, respectively). The carbon and nitrogen in plant pools enter soil pools with the mortality of
292 individual trees and the turnover of leaves and fine roots. Soil has a mineral nitrogen pool for
293 mineralized nitrogen and five soil organic matter (SOM) pools for carbon and nitrogen:
294 metabolic litter (x_1), structural litter (x_2), microbial (x_3), and fast (x_4) and slow-turnover (x_5) SOM
295 pools.

296 The microbial pool plays a central role in the transfer and decomposition of SOM. The
297 decomposition processes are simulated by a model modified from Manzoni et al. (2010). The
298 technical details have been described in detail in Weng et al. (2019, 2017). The decomposition
299 rate of a SOM pool is determined by the basal turnover rate together with soil temperature and
300 moisture following the formulation of the CENTURY model. The microbial carbon use
301 efficiency (transfer from litter to microbial matter) is a function of litter nitrogen content,
302 following the model of Mazoni et al. (2010).

303 The N mineralization in decomposition is determined by microbial nitrogen demand,
304 SOM's C:N ratio, and decomposition rate. In the high C:N ratio SOM, microbes must consume
305 excess carbon to get enough nitrogen for growth. By contrast, in the low C:N ratio SOM,
306 microbes must release excess nitrogen to get enough carbon for energy. Depending on the C:N
307 ratios of SOM, soil microbes may be limited by either C or N.



308 The out-fluxes of C and N from the i^{th} pool (dC_i and dN_i , respectively) are calculated by:

$$dC_i = \xi(T, M)\rho_i Q C_i, \quad (11)$$

$$dN_i = \xi(T, M)\rho_i Q N_i,$$

309 where ξ is the response function of decomposition to soil temperature (T) and moisture (M), ρ_i is
310 the basal turnover rate of the i^{th} litter pool at reference temperature and moisture, $Q C_i$ is the C
311 content in i^{th} pool, and $Q N_i$ is the N content in the i^{th} pool.

312 The new microbial growth (dM) is calculated as the co-limit of available carbon and
313 nitrogen mobilized at this step:

$$dM_i = \text{Min}(\varepsilon_0 \cdot dC_i, \Lambda_{\text{microbe}} \cdot dN_i), \quad (12)$$

314 where ε_0 is default carbon-use efficiency of litter decomposition (0.4) and Λ_{microbe} is a microbe's
315 C:N ratio, which is a fixed value (10 in this model). The soil heterotrophic respiration (R_h) is the
316 microbial respiration (i.e., the difference between carbon consumption and new microbial
317 growth), and the total N mineralization rate ($N_{\text{mineralized}}$) is calculated as the sum of mineralized N
318 in the SOM pools and microbial turnover:

$$R_h = \sum_{i=3}^5 dC_i - \sum_{i=4}^5 M_i, \quad (13)$$

$$N_{\text{mineralized}} = \sum_{i=3}^5 dN_i - \sum_{i=3}^5 m_i / \Lambda_{\text{microbe}}$$

319 The R_h releases to atmosphere as CO₂. Mineralized N enters the mineral N pool for plants to use.
320 The dynamics of the mineral N pool is represented by the following equation:

$$\frac{dN_{\text{mineral}}}{dt} = N_{\text{deposition}} + N_{\text{mineralized}} - U - N_{\text{loss}}, \quad (14)$$

321 where $N_{\text{deposition}}$ is N deposition rate, assumed to be constant over the period of simulation; N_m is
322 the N mineralization rate of the litter pools (fast and slow SOM and microbes); U is the N uptake
323 rate (Kg N m⁻² hour⁻¹) of plant roots; and N_{loss} includes the loss of mineralized N by



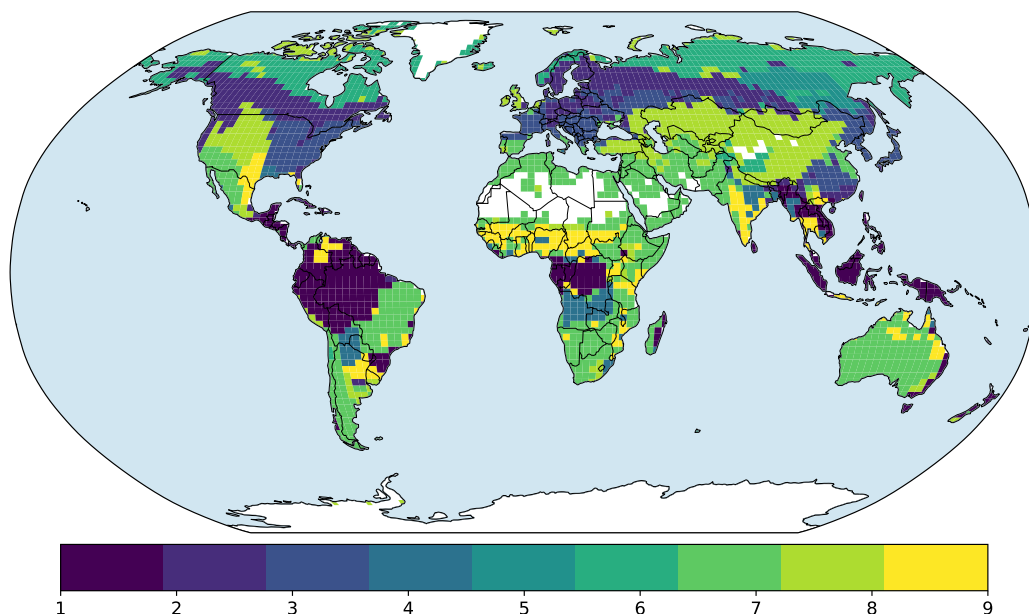
324 denitrification and runoff. The N deposition ($N_{\text{deposition}}$) is the only N input to ecosystems, and we
325 set nitrogen fixation as zero in this version of the model.

326

327 **3 Model Test runs**

328 For our comparison of model performance against observations and other models, we used
329 the full demographic version of BiomeE (described above) and also designed a “single-cohort”
330 version of the model to benchmark our demographic implementations. In the single-cohort
331 model, the mortality of trees is simulated as the turnover of woody biomass, and the fecundity
332 resources (carbon and nitrogen) are used to build the same-sized parent trees, instead of
333 seedlings growing from understory layers. If the total crown area of the trees in this cohort is
334 greater than the land area, the extra trees will be removed to make the total crown area less than
335 or equal to the land area. At equilibrium, the turnover of wood biomass is equal to the new
336 growth each year and the new trees generated from fecundity resources are to be killed by self-
337 thinning. The single-cohort model uses the mean state of the canopy layer trees to represent the
338 characteristics of the whole community. This single-cohort model performs like the traditional
339 biogeochemical models and simplifies vegetation computation.

340 In the test runs, the distribution of PFTs was from the Ent vegetation map (Ito et al., 2020),
341 which is derived from 2004 MODIS land cover and PFT data products (Friedl et al., 2010) and
342 climate data (Fig. 2). For these simulations, croplands and pastures were replaced by the
343 potential natural vegetation types.



344

345 **Figure 2 Prescribed global distribution of plant functional types.** Data is from the Ent Global
346 Vegetation Structure map. The numbers are corresponding to the PFTs in Table 1.

347

348 Forcing data are from TRENDY project CRU-NCEP data (Sitch et al., 2015) and have a 6-

349 hour time step at a spatial resolution of $0.5^\circ \times 0.5^\circ$. These data are available at the website

350 <https://www.uea.ac.uk/web/groups-and-centres/climatic-research-unit/data>.

351 We aggregated these data into $2.0^\circ \times 2.5^\circ$ grid cells and used thirty years' data (1988~2017) to

352 force the model to run for 600 years, which is long enough for the model to approach equilibrium

353 states for both vegetation and soil carbon pools. These data include temperature, precipitation,

354 shortwave radiation, longwave radiation, specific humidity, and wind speed (U and V

355 directions). The interpolation of radiation (R) is based on the zenith angle (θ_s) and penetration

356 rate calculated from the 6-hour step data.



$$R_S(t) = \left(\frac{R_{H6}}{S^* \cos \theta_s(H6)} \right) S^* \cos \theta_s(t), \quad (15)$$

357 where S^* is solar constant (1362 W/m^2). Other variables are linearly interpolated to the model
358 time steps, which is half hourly in this study. CO_2 concentration is set at the model default level
359 (350 ppm) in our model runs.

360 **Data sources for model evaluation**

361 **Gross primary productivity (GPP) data** are from a global retrieval of surface turbulent fluxes
362 including latent heat, sensible heat, and GPP using remote sensing observations. These data are
363 on a $1^\circ \times 1^\circ$ geographic grid at a monthly time step based on an Artificial Neural Network
364 retrieval algorithm (Alemohammad et al., 2017). This algorithm uses six remotely sensed
365 observations as input: Solar Induced Fluorescence (SIF), Air Temperature, Precipitation, Net
366 Radiation, Soil Moisture, and Snow Water Equivalent. The data are available from 2007 to 2015.

367 **The tree height data** are from spaceborne light detection and ranging (lidar) global map of
368 canopy height at 1-km spatial resolution developed by Simard et al. (2011). These authors used
369 the 2005 data from the Geoscience Laser Altimeter System (GLAS) aboard ICESat (Ice, Cloud,
370 and land Elevation Satellite) to derive global forest canopy heights. **Biomass data** are from a
371 Global 1-degree Maps of Forest Area, Carbon Stocks, and Biomass, 1950-2010 developed by
372 Hengeveld et al. (2015). **Soil carbon data** are from Food and Agriculture Organization (FAO)
373 Harmonized World Soil Database (version 1.2), updated by Wieder et al. (2014).

374 **MsTMIP model simulation data**

375 We chose six model simulations (BiomeBGC, CTEM, CLM4, LPJ, Orchidee, VEGAS) from the
376 Multi-scale Synthesis and Terrestrial Model Intercomparison Project (MsTMIP) (Huntzinger et
377 al., 2012) to compare against our model simulations. These models are well-developed and



378 widely used in Earth system models, representing the state-of-art of current land vegetation
379 model development.

380 Selected Grid Cells for Comparison

381 For illustrating model behavior, we selected 8 grid cells that cover boreal forests, temperate
382 forests, tropical forests, C₄ grass, and arid shrubs to show the simulated ecosystem development
383 patterns across the climate zones with different dominant PFTs (Table 2). Brazil Tapajos (TPJ),
384 Oak Ridge (OKR), Harvard Forest (HF), Manitoba old black spruce site (MNT), and Bonanza
385 Creek (BNC) are covered by tree PFTs. Konza long-term ecological research station (LTER)
386 (KZ) is C₄ grass. Walnut Gulch Kendall (WKG) and Sevilleta LTER (SV) are covered by arid
387 shrubs. These sites were chosen because they have extensive data on vegetation and climate
388 conditions for future comparisons.

389

390 **Table 2 Grids for simulated ecosystem development illustration**

Grid	Dominant PFT	Coordination	Mean Temperature (°C)	Annual Precipitation (mm)
Bonanza Creek (BNC)	Broadleaf deciduous	63.92°, -145.38°	-3.1	269
Manitoba old black spruce site (MNT)	Evergreen needleleaf	55.88°, -98.48°	-3.2	520
Harvard Forest (HF)	Broadleaf deciduous	42.54°, -72.17°	8.5	1050
Oak Ridge (OKR)	Broadleaf deciduous	35.96°, -84.29°	13.7	1372
Konza LTER (KZ)	C ₄ grass	39.08°, -96.56°	12.4	835
Sevilleta LTER (SV)	Arid shrub	34.36°, -106.88°	12.7	365
Walnut Gulch Kendall (WKG)	Arid shrub	31.74°, -109.94°	17.7	350
Brazil Tapajos (TPJ)	Broadleaf evergreen	-2.86°, -54.96°	26	1820

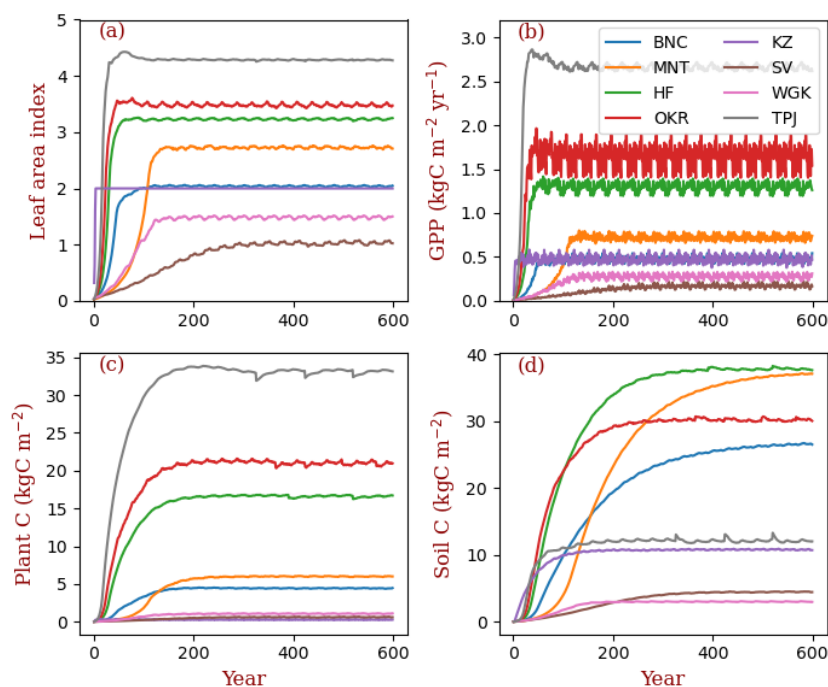
391



392 4 Results

393 4.1 Simulated ecosystem dynamics in different climate zones

394 Across all the 8 sites, GPP aligns closely with LAI in the full demographic simulations
395 (Fig. 3), with forested sites having, overall, higher LAI, biomass, and carbon stocks per area
396 compared to the shrub and grass sites. Vegetation biomass is lowest at the grassland site (i.e.,
397 KZ) because, within the model, grassland ecosystems cannot accumulate persistent woody
398 biomass.

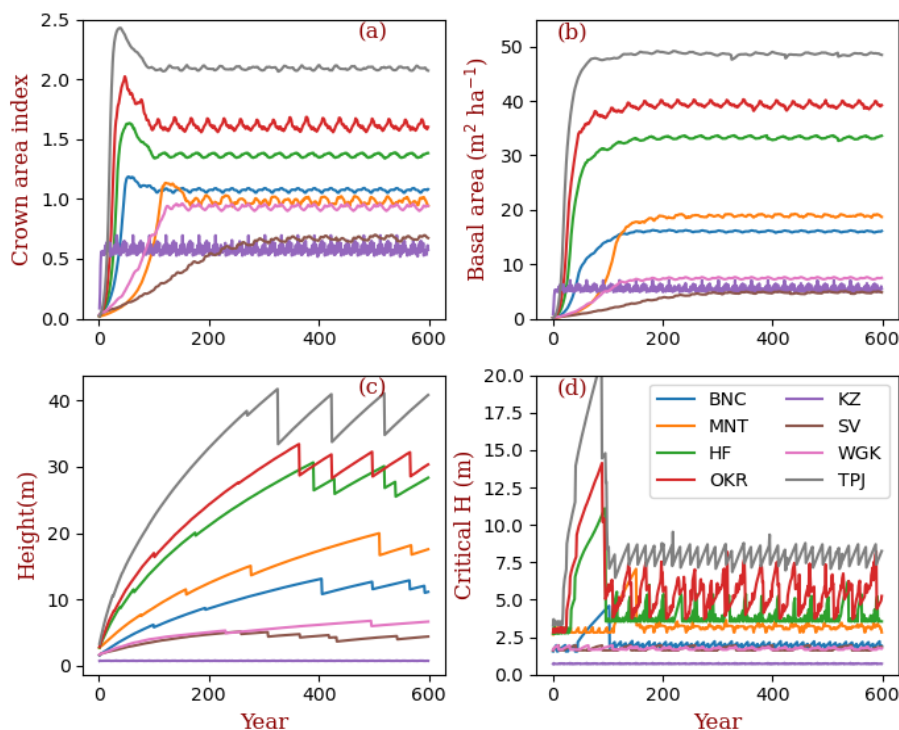


399

400

401

Figure 3: Site ecosystem development simulated by BiomeE with full demography.



402

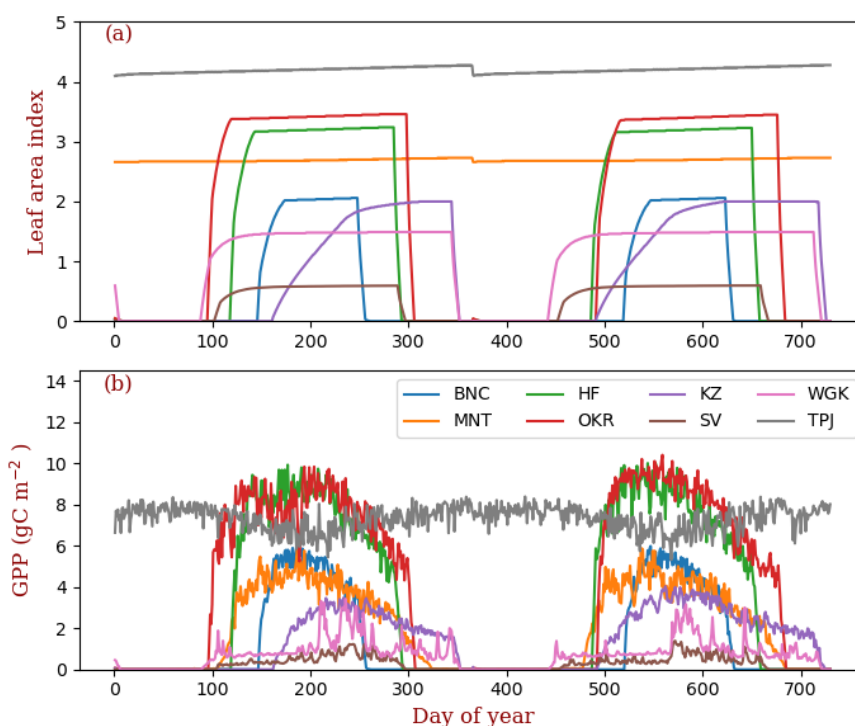
403 **Figure 4. Vegetation structural dynamics.** Critical height (H) is an emergent property of the
404 model PPA, which separates the trees that are in full sun light if taller than critical height and
405 those that are fully shaded if shorter than critical height.

406

407 The tropical forest site (TPJ) has the highest crown area index (around 2.2), followed by
408 warm temperate forest at OKR, mixed forest at HF, and boreal forests at BNC and MNT (Fig. 4).
409 The shrubs and grasslands in arid regions have the lowest crown area index (CAI), with basal
410 area following similar patterns. For forested sites, tree height is tallest at TPJ, followed by OKR,
411 HF, MNT, and BNC. The shrubs are short according to their allometry parameters and the height
412 of grasses during non-growing season is zero. The critical height, which separates canopy layer
413 trees from the understory layers, follow the same order as that of tree height with high
414 fluctuations with cohort changes. Equilibrium time scales for LAI and GPP are similar across



415 sites, but biomass accumulation is much slower in forests because of the longer time needed for
416 forest structure (size distribution) to approach equilibrium. Soil carbon equilibration is faster in
417 the warm regions than in cold regions because of the high turnover rate of SOM pools in warm
418 regions.
419

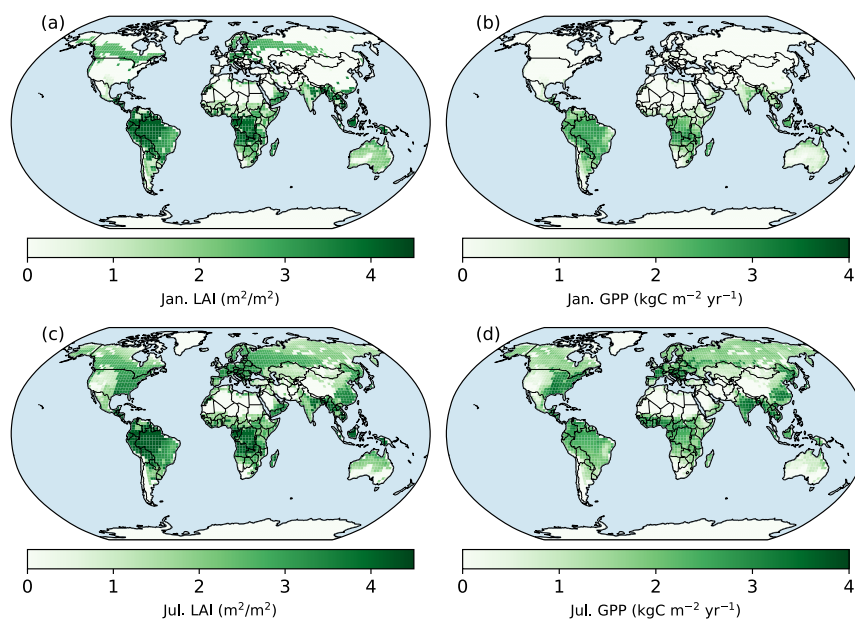


420
421 **Figure 5. Seasonal patterns of LAI and gross primary production in the sample grids.** Two
422 years of data are shown in this figure. The key of location abbreviations is in Table 2.

423
424 The PFTs at TPJ and MNT are evergreen forest. Their LAI does not change over the whole
425 year (Fig. 5: a). The forest in OKR has the longest growing season in the three deciduous forest
426 grids, followed by HF and BNC. BNC's growing season is only around 120 days, about half of
427 OKR's growing season. The growing season of grasses in KZ starts in late May and ends in



428 September. The two arid-adapted shrub sites (SV and WKG) are controlled by water availability.
429 In TPJ (tropical evergreen forest), the trees have photosynthesis throughout the entire year (Fig.
430 5: b). In MNT, photosynthesis only happens in warm seasons with the leaves kept in the crowns
431 (evergreen needleleaf). The deciduous trees in OKR and HF have high photosynthesis rates
432 during the growing season. The photosynthesis rates in SV and WKG are generally low because
433 of the drought environment. However, the precipitation events can drive photosynthesis rates
434 high in these arid regions. At the global spatial scale, only evergreen needle-leaved forests keep
435 their leaves in northern high latitude regions during January (Fig. 6). The photosynthesis of
436 plants in this region is off because of the low temperature. In July, northern high latitude regions
437 green up and their photosynthesis rates are high in wet regions.
438



439
440 **Figure 6. Spatial patterns of LAI and GPP in Jan and July.** Panels a and b are the LAI and
441 photosynthesis of January in the year of 600 (the last year of model run). Panels c and d are
442 July's in the same year.

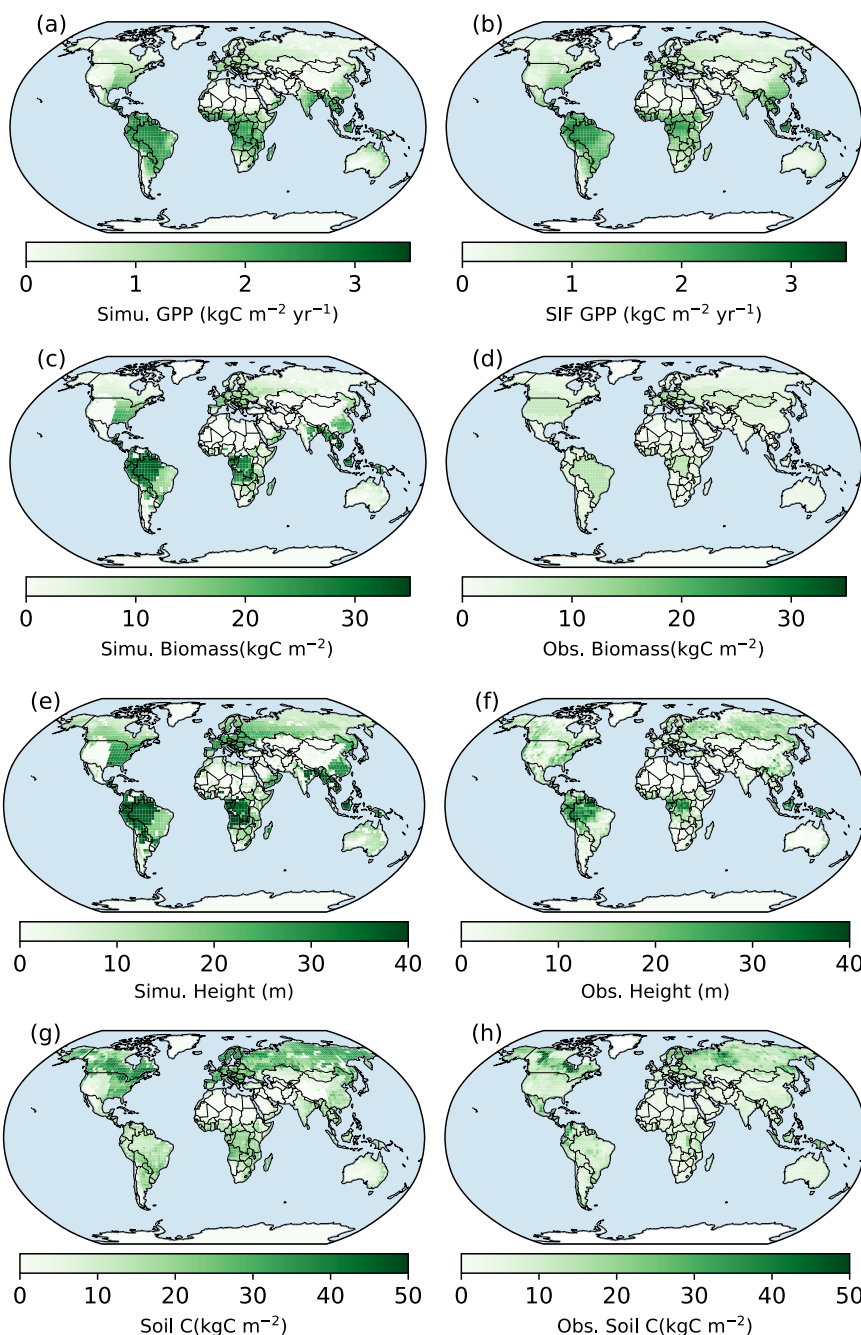


443

444 **4.2 Global Comparisons with Observations**

445 We tuned the parameter of maximum carboxylation rate (V_{cmax}) to fit the general pattern of
446 global GPP. Compared with SIF GPP (Alemohammad et al., 2017), simulated GPP is higher than
447 the SIF GPP generally (Figs. 7 and 8), though lower in arid regions (Fig. 7). The simulated tree
448 height is mostly taller compared to observations (Simard et al., 2011) because most forests have
449 been altered by human activities (Pan et al., 2013). However, the model and observations cover
450 approximately the same range of tree heights (up to 40 m). Simulated biomass is much higher
451 than the observations because most forest regions have been transformed to low biomass land
452 use types or represent earlier successional stages with less accumulated carbon (i.e., not
453 equilibrium states). Simulated soil carbon does track the observations better than biomass, likely
454 because soil carbon stocks are more stable compared to biomass. For areas where the model
455 underpredicts soil carbon, the difference could arise because of missing processes that may lead
456 to high accumulation in some regions (e.g., peats) or the relatively high uncertainties in the soil
457 carbon data (Tifafi et al., 2018).

458



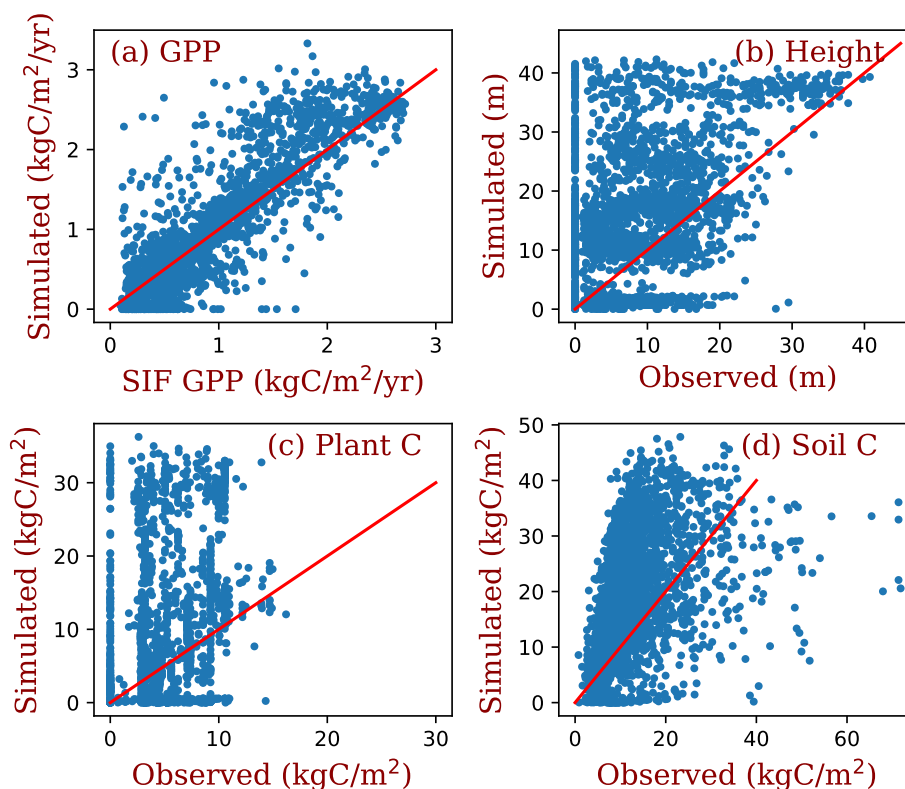
459

460

461 **Figure 7. Spatial patterns of BiomeE (full demography) simulations and those from data.**
462 “Obs.” means different way retrieved from observations. Some are model-based (e.g., GPP is



463 from SIF data and tree height is from LiDAR data). Obs. **GPP** is derived from Solar Induced
464 Fluorescence (SIF) data with a machine learning approach (Alemohammad et al., 2017). The
465 data are available from Jan. 2007 to Dec. 2015. **The tree height data** are from spaceborne light
466 detection and ranging (lidar) global map of canopy height at 1-km spatial resolution developed
467 by Simard et al. (2011). **Biomass data** are from Hengeveld et al. (2015). **Soil carbon data** are
468 from FAO Harmonized World Soil Database (version 1.2), updated by Wieder et al. (2014).
469



470
471 **Figure 8** Grid comparison of full demographic BiomeE simulations with observations
472 estimates. The red line in each panel is the 1:1 line. This figure uses the same simulated and
473 observed data as those of Figure 7.

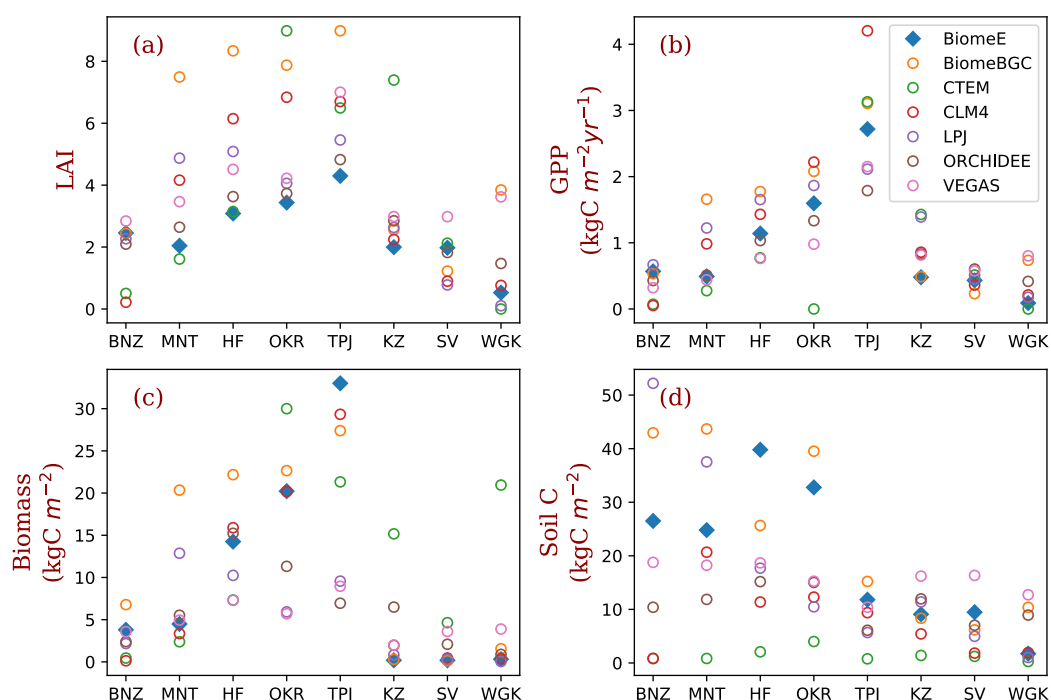
474

475 4.3 Comparison with MsTMIP models

476 We compared the performance of our model with MsTMIP models at the 8 locations that
477 were used to show ecosystem development patterns (Table 2). For most of these sites, LAI in



478 BiomeE is lower compared the other MsTMIP models (Fig. 9: a), while the estimated GPP is
479 centered in within the range of MsTMIP predictions (Fig. 9: b). Differences are a consequence
480 of the formulations within BiomeE. Specifically, BiomeE simulates leaf growth by using a
481 maximum crown LAI, which is lower than the real forest LAI. However, the low LAI does not
482 affect crown total photosynthesis because leaves in lower canopy layers contribute little to the
483 total carbon assimilation. BiomeE predicted biomass (Fig. 9: c) and soil carbon (Fig. 9: d)
484 generally fall towards the higher end of the MsTMIP simulations, except for the more arid grass-
485 and shrub-dominated sites. We note, however, that there are wide differences in estimates for
486 vegetation and soil carbon across the models, likely because of different treatments of mortality
487 and decomposition functions in these models.



488

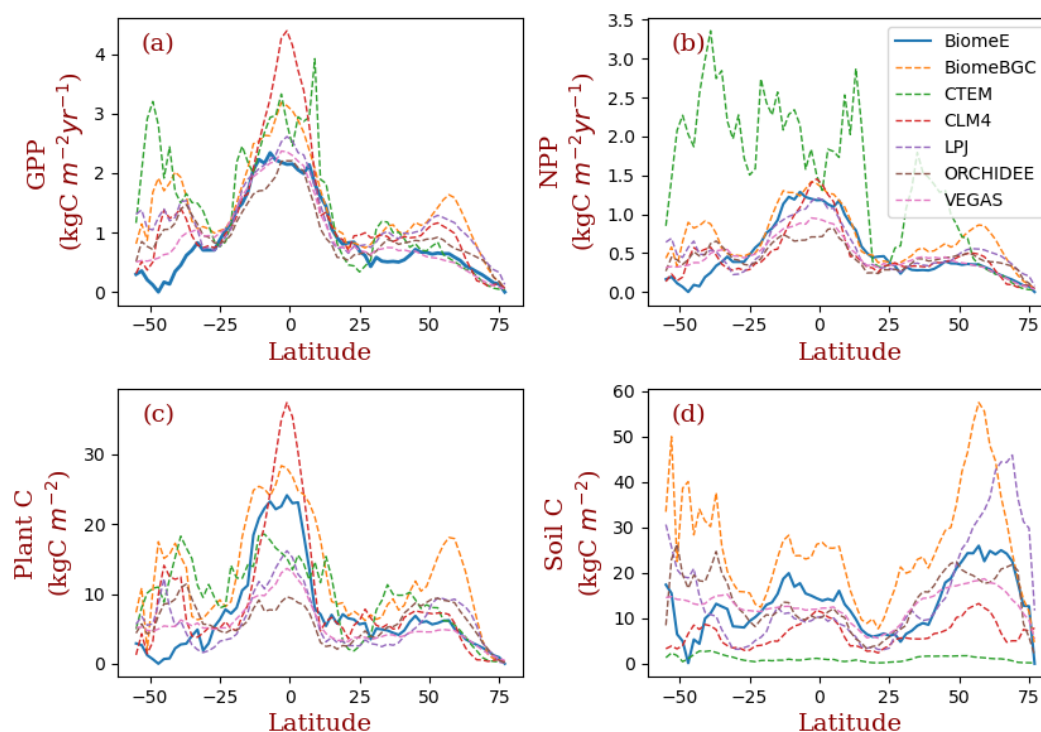
489

Figure 9 Site-level comparison with MsTMIP models.



490 The BiomeE predictions are from the model version with full demography. The abbreviations of
491 the 8 sites (corresponding to model grid cells) and their coordination, dominant PFTs, and
492 climatic conditions are in Table 2.

493



494

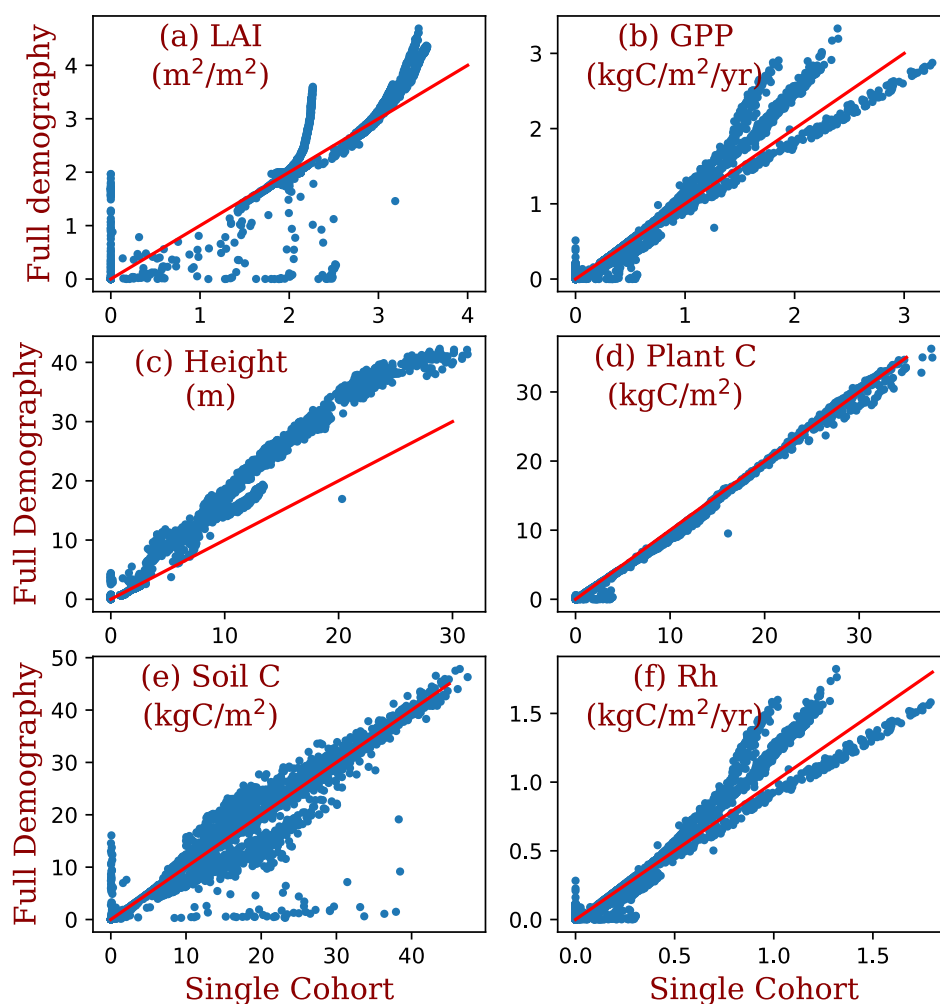
495 **Figure 10** Latitudinal patterns of GPP, NPP, Biomass, and soil carbon as simulated by
496 **BiomeE (with full demography) and MsTMIP models**

497

498 More broadly, the latitudinal mean of BiomeE simulated GPP is at the lower end of MsTMIP
499 model predictions (Fig. 10: a). Since BiomeE's GPP was tuned to fit remote sensing data derived
500 GPP, the MsTMIP models may over-estimate global GPP. BiomeE simulated NPP (Fig. 10: b),
501 plant carbon (Fig. 10: c), and soil carbon (Fig. 10: d) are within the range simulated by the
502 MsTMIP models. This indicates that BiomeE has slightly lower respiration than the MsTMIP



503 models. In the arid regions (e.g., around latitude 40-50° S), our model's GPP is lower than
504 MsTMIP's because of sensitive drought responses in our model.
505



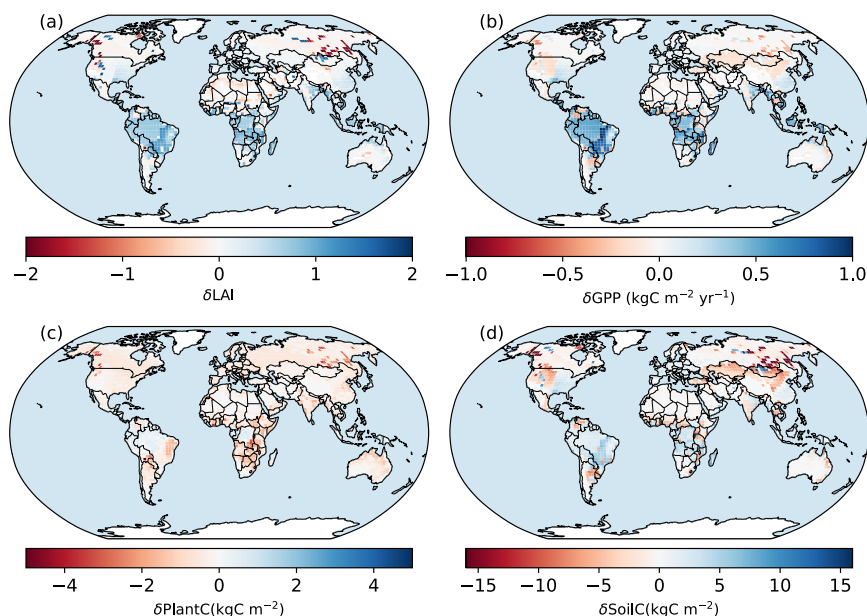
506
507 **Figure 11 Comparison between the simulations of the full demography and the single**
508 **cohort settings of BiomeE.**

509
510 The demographic processes have significant impacts on the simulations of GPP, biomass, soil
511 carbon, and vegetation structure compared to the single-cohort version of BiomeE (Fig. 11). The



512 demographic version of the model includes an understory layer of plants, resulting in higher LAI
513 in high LAI regions and also slightly higher GPP. Higher GPP in the model with full
514 demography leads to a high allocation to leaves and fine roots. However, the total biomass
515 predicted by the two model versions are similar because of the tradeoffs in allocation between
516 leaves and stem growth and tree size distribution and because most biomass is concentrated in
517 stems. In the full demography model, tree mortality removes all the biomass, including leaves,
518 fine roots, and stems, while in the single-cohort model, the mortality is represented as the
519 turnover of woody biomass. Consequently, the full demography model has higher emergent
520 turnover rate for the whole vegetation.

521 Compared to the single-cohort model, the full demography model predicts higher LAI and
522 GPP in warm and wet regions and lower values in cold and dry regions (Fig. 12: a, b). The full
523 demography model also predicts much lower biomass and soil carbon than the single-cohort
524 model in cold and dry regions (Fig. 12: c). Because the single cohort model has the same SOM
525 pools and turnover/decomposition processes, the reduced biomass input from full demography
526 alone is causing the difference in SOM dynamics. This is consistent with the functions of
527 demographic processes in these regions, which greatly reduce model stability because
528 reproduction and survival are lower in dry and cold regions. By contrast, the single-cohort model
529 does not model these processes explicitly and instead uses a simplified routine turnover of
530 materials that allows plants to stay in extremely dry or cold conditions.



531

532 **Figure 12** Spatial patterns of the differences between the simulations of the BiomeE with full
533 demography and with the single-cohort settings.

534

535 **5 Discussion**

536 We developed BiomeE, a parsimonious terrestrial ecosystem model for ModelE, to simulate
537 vegetation dynamics and biogeochemical cycles. This model includes a cohort-based
538 representation of vegetation structure, a height structured light competition scheme, demographic
539 processes, and coupled carbon-nitrogen biogeochemical cycles. This model has four major
540 modules that organize the hierarchical processes of ecosystems together into a cohesive
541 modeling structure: 1) plant physiology (photosynthesis, respiration), 2) plant phenology and
542 growth, 3) vegetation structural dynamics, and 4) soil biogeochemical cycles (Fig. 1). Each
543 module is cohesive and has a minimum set of variables as the input from other modules.

544



545 5.1 Model formulation

546 In designing this model, we considered the simulation of competitively optimal strategy of
547 plants in different climates based on fundamental ecological rules (Purves and Pacala, 2008;
548 Falster and Westoby, 2003; Franklin et al., 2020). These strategies are mainly related to light
549 competition, water conditions, nutrient use efficiency, and disturbances (e.g., fire), and
550 represented by the traits of wood density, height growth, leaf longevity, and photosynthesis
551 pathways. PFTs are used in this model as an integrative unit representing combinations of plant
552 traits for simulating (1) the spontaneous dynamics of carbon, water, and energy fluxes as the core
553 functions of an ESM-based land model and (2) the transient vegetation structural and
554 compositional dynamics and ecosystem biogeochemical cycles in response to climate variations.
555 We adopted a generic design for the PFTs in the standalone BiomeE (Weng et al., 2019): since
556 the PFTs are samples of plant traits in their natural ranges, the numbers of PFTs are flexible,
557 depending on what strategies users wish to test. This approach substantially simplifies the
558 parameterization of PFTs because it changes the parametrizations to the selections of strategies
559 through choosing different trait values (i.e., parameters). Thus, the PFTs are adaptive and can
560 change to each other in different climate zones, making it possible to reduce the number of PFTs
561 while representing functional diversity and the optimal adaptation to climate conditions.

562 To represent the major variations in plant functional diversity, we chose four plant traits as
563 the primary axes to define PFTs: wood density, leaf mass per unit area (LMA), height growth
564 parameter, and leaf maximum carboxylation rate (V_{cmax}). Wood density is relatively conservative
565 (Swenson and Enquist, 2007; Chave et al., 2009), mostly ranging from 200 to 500 kg C m⁻³,
566 while herbaceous stem density ranges from 400~600 kg C m⁻³ (Niklas, 1995). However,
567 herbaceous stems are usually hollow, making the ratio of total biomass to its volume low, and



568 grasses shed their stems each growing season, resulting in faster stem turnover. It is a strategic
569 difference from woody plants, which keep the woody tissues to build up their trunks and thus
570 display their leaves on top of trunks for light competition (Dieckmann et al., 2007; Falster and
571 Westoby, 2003). LMA is the key leaf trait that determines leaf life longevity and leaf types (i.e.,
572 evergreen vs. deciduous) (Osnas et al., 2013), and represents the strategy for the competition in
573 different soil nutrient levels (Tilman, 1988; Reich, 2014; Weng et al., 2017) and resistance to
574 stresses of water and temperature (Oliveira et al., 2021).

575 In this model, the phenological type is simulated as an emergent property of plant
576 physiological processes and its strategy to deal with seasonal variations of temperature and water
577 availability. We used three parameters – growing degree days (GDD), running mean daily
578 temperature, and critical soil moisture – to define all possible phenological types. These three
579 parameters are widely used in a variety of phenology models (Sitch et al., 2003; Prentice et al.,
580 1992; Arora and Boer, 2005). As for soil organic matter decomposition, the CASA model is
581 currently used in ModelE; it has 13 pools with different transfer coefficients and turnover rates
582 (Randerson et al., 1997; Potter et al., 1993, 2003). The models developed thereafter have more
583 sophisticated processes, especially those of microbial activities and carbon use efficiency
584 (Manzoni et al., 2010; Wieder et al., 2014; Wang and Goll, 2021). We chose an intermediate
585 complexity scheme that has only two SOM pools but a functional microbial pool for
586 decomposing SOM so that the dynamics of SOM's C/N ratio, carbon use efficiency, and nitrogen
587 mineralization can be reasonably simulated while keeping the model structure parsimonious.

588

589 **5.2 Model predictions and performance**



590 This model has four relatively distinctive sets of simulated variables that are critical for model
591 performance and calibration: 1) Stomatal conductance, photosynthesis, and respiration; 2)
592 demographic rates (i.e., allocation, structural growth, mortality, and reproduction); 3) LAI, tree
593 size, crown self-organization, and vegetation structure; 4) Soil carbon and nitrogen storage. In
594 this paper, we only evaluated the carbon cycle in the model simulations, though the nitrogen
595 cycle is also simulated in tandem with the carbon cycle in the model. We did not extensively
596 tune model parameters to fit observations because the purpose of this paper is to describe the
597 formulation of the model. The core processes of this model, e.g., photosynthesis, respiration,
598 phenology, growth, allocation, demography, soil biogeochemical cycles, are from well-
599 developed models and have been shown able to capture observational patterns. Data assimilation
600 approaches can be implemented when parameter tuning becomes essential.

601 The simulations demonstrate that this model can capture global patterns of GPP, LAI, tree
602 height, biomass, and soil carbon, even though the parameters are not extensively tuned. For
603 example, global GPP patterns are consistent with those derived from SIF data (Fig.7: a, b and
604 Fig. 8: a), and simulated tree heights span the same ranges of those derived from data. The
605 simulated biomass and soil carbon is generally higher than in observations, though simulated soil
606 carbon is lower in some cold regions. Several factors likely explain the apparent overestimates of
607 GPP, biomass, and soil carbon in the model. First, the model uses a potential PFT distribution
608 and does not account for land cover change and land use history. For example, carbon dense
609 ecosystems (e.g., forests) have been extensively replaced by croplands and pastures. Second,
610 while vegetation in the real world reflects a variety of successional stages and the effect of
611 various disturbance events, our model analyses are based on equilibrium simulations without
612 explicit disturbances, such as fire, deforestation and regrowth. Third, the model assumes mineral



613 nitrogen is saturated and can consistently meet demands for plant growth. We did not fix the land
614 cover mismatches by compromising ecosystem physiological processes because we cannot put
615 all these effects into current model structure (i.e., mortality) when many processes are missing.

616 LAI is an illustrative variable for understanding why compromises are necessary when
617 integrating ecologically based vegetation models into ESMs. LAI, as a critical prognostic
618 variable in vegetation models, links both plant physiology and biogeophysical interactions with
619 climate systems. While LAI is usually simulated by a fixed allocation scheme, even if the
620 allocation ratios are dynamic with vegetation productivity (Montané et al., 2017), the prediction
621 of LAI in models is often simplified as the balance between growth and turnover. Modelers tend
622 to tune LAI to fit observations and get the required albedo and water fluxes whatever their
623 parameters of photosynthesis and respirations are. This LAI usually makes the lower layer
624 leaves carbon negative. However, a first principle is that a tree should have an optimal LAI to
625 maximize its carbon gain as a result of crown structure, light interception, and community-level
626 competition (Anten, 2002; Hikosaka and Anten, 2012; Niinemets and Anten, 2009). Thus, in our
627 model, we defined a much lower target LAI due to the assumption of the uniform the leaves
628 within a crown to avoid carbon negative leaves.

629 The leaf traits in the crown profile should, in reality, be a function of light, water and
630 nitrogen (Niinemets et al., 2015). This “uniform leaf” assumption makes the lower layer leaves
631 carbon negative when LAI is tuned close to that observed in tropical and boreal evergreen forests
632 (where LAI is around 5~7). Thus, the photosynthesis rate must be tuned to fit the canopy
633 photosynthesis by keeping the carbon negative leaves. However, the carbon negative leaves do
634 not affect ecosystem dynamics in the “single-cohort” models because the whole canopy net
635 carbon gain is still reasonable and can be fitted to the observed dynamics. This contrasts with the



636 demographic version of the model, which represents trees with different sizes and in different
637 layers and creates conditions where seedlings in the understory cannot survive because of light
638 limitation and negative carbon balances in some dry and cold regions.

639 The leaf maximum carboxylation rate (V_{cmax}) used in this model is also much lower than
640 measured in young leaves (Bonan et al., 2011) because the aging of leaves is considered in the
641 mean value of V_{cmax} of all leaves with different ages. The mean V_{cmax} of the whole canopy leaves
642 is much lower than the new leaves that are usually used to measure V_{cmax} . If the leaves were not
643 specifically chosen, the mean of measured V_{cmax} is much lower than those used in models as
644 shown in Verryckt et al. (2022). This also indicates that V_{cmax} in current vegetation models is
645 over-estimated.

646 The allometry of plant architecture, rules for plant growth, and reproduction and mortality
647 processes form the basis of vegetation structural dynamics. The formulation of allometry makes
648 the whole-tree's photosynthesis and respiration proportional to crown area, and thus the growth
649 rate of tree diameter independent of crown area. These vital rates drive vegetation structural
650 changes and biogeochemical cycles (Purves et al., 2008). Our model makes it possible to
651 simulate vegetation composition and structural dynamics based on the fundamental principles of
652 ecology, and the transient changes in terrestrial ecosystem in response to climate change. This
653 model therefore has the potential to predict competitively dominant strategies represented by
654 plastic plant traits (e.g., leaf traits, allocation etc.), resulting in simulated vegetation structure and
655 composition that will be eco-evolutionarily optimized. PPA defines the height-structured
656 competition for light. The allocation scheme between the growth of stems and functional tissues
657 (i.e., leaves and fine roots) is the strategy of resources foraging for light and soil resources.

658



659 **5.3 Major uncertainties in this model**

660 We used many simplifying assumptions to organize ecosystem processes at different scales into
661 a cohesive model structure that balances the complexity of different processes and our
662 knowledge. For example, some processes are based on well-understood physical processes and
663 mathematical derivation, including, the photosynthesis model (FVC) (Farquhar et al., 1980),
664 respiration responses to temperature (Arrhenius equation), and height-structured light
665 competition (i.e., PPA) (Strigul et al., 2008). Many other processes, such as phenology, drought
666 effects, however, are phenomenological equations representing the poorly understood links
667 between processes needed to allow the model to simulate the entire system. In the following
668 sections, we highlight these assumptions and evaluate their relative benefits and costs.
669 Transparency in the description of a community model such as this one will help future
670 developers understand compromises and areas that can be improved with new information or
671 approaches. The following phenomenological relationships represent the major sources of
672 uncertainty in this model.

673 Water limitation of photosynthesis is calculated as a function of relative soil moisture
674 following the water stress function from Rodriguez-Iturbe et al. (1999):

$$\beta_D = \text{Min} \left(1.0, \max \left(\frac{s_D - s_{\min}}{s^* - s_{\min}}, 0.0 \right) \right), \quad (16)$$

675 The parameters s^* and s_{\min} are PFT-specific, representing different responses of PFTs to soil
676 water conditions, and S_D is the relative soil moisture ranging from 0 (soil water content at wilting
677 point) to 1 (at field capacity). This formulation that scales soil moisture to a scalar between zero
678 to 1 is repeatedly used in both physiological responses of photosynthesis and phenology in
679 ecosystem models as a simplistic treatment of the central role of water limitation on plant



680 physiology (Harper et al., 2021; De Kauwe et al., 2015; Powell et al., 2013). This equation does
681 not include the detailed processes of plant hydraulics and its adaptation to arid environments.

682 Plants have multiple tradeoffs and strategies to improve their competitiveness under water
683 stress, such as regulating stomata conductance, shedding leaves, producing more roots, etc.
684 (Oliveira et al., 2021; Volaire, 2018). At the ecosystem level, competition and evolutionary
685 processes filter community emergent properties (Franklin et al., 2020; van der Molen et al.,
686 2011). For example, trees in different climate regions have similar hydraulic safety margin
687 (Choat et al., 2012), partly due to the intense competition for light (height growth) and water
688 (root allocation) that require optimal use of available resources at any climate conditions
689 (Gleason et al., 2017; Liu et al., 2019). However, in this model, the drought responses are only
690 delineated by the Eq. 16. The parameter choices for s^* and s_{\min} likely explain the amplified water
691 stresses and low productivity in arid regions within our model.

692 Phenology represents the seasonal rhythms of plant physiological activities as adapted to
693 periodic changes in temperature, precipitation, and light availability (Abramoff and Finzi, 2015;
694 Caldararu et al., 2014; Chuine, 2010). DGVMs normally simulate leaf onset and senescence
695 based on temperature conditions for cold deciduous plants and soil water conditions for drought
696 deciduous plants (Arora and Boer, 2005; Caldararu et al., 2014). Phenology modeling is still
697 highly empirical, although new models and approaches for cold deciduous and drought
698 deciduous strategies have been proposed recently (e.g., Caldararu et al., 2014; Chen et al., 2016;
699 Dahlin et al., 2015; Manzoni et al., 2015). We used a simple formulation of temperature (Eqs 1
700 and 3) and drought responses. For the cold-deciduous strategies, the phenology model balances
701 growing season length and frost risks by adjusting critical GDD0 and T0 according to chilling
702 days and growing days to reduce frost risk in warm regions and increase growing season length



703 in cold regions. In this way, leaf senescence also considers growing season length and leaf aging.
704 For example, in areas with longer growing seasons, plants will have a higher T_0 and initiate
705 senescence at higher temperatures. For the drought phenology, we set different critical soil
706 moisture indexes to initiate and terminate a growing season (Table 1). However, these
707 relationships are phenomenological, and ecological rules will benefit future model development.

708 Mortality is an integrative result of accumulative physiological stresses, structural
709 damages, and disturbances during a tree's lifetime. The direct reasons can be starvation,
710 structural failure, hydraulic failure, etc. (McDowell, 2011; Aakala et al., 2012; Aleixo et al.,
711 2019). In this model, we only consider the background mortality and define its rate as a function
712 of tree diameter and light environment (Eq. 10). Hydraulic failure-induced mortality is required
713 for studying plant responses to climate changes.

714 We employed these general phenomenological equations primarily because more
715 mechanistic equations are not currently known. In addition, our interest is to keep this model as
716 simple as possible to improve interpretability and transparency and to reduce the computational
717 burden when it is integrated into the ModelE. In these places where the tradeoff between model
718 complexity and process accuracy is necessary, we highlight the underlying assumptions clearly,
719 rather than applying temporary fixes not based on solid ecological modeling approaches.

720 Generally, we are using the key variables that characterize ecosystem properties to define
721 the basic model structure but have to use less-than-solid information to link them together by
722 phenomenological relationships, as all the models do. The enduring issues in vegetation
723 modeling as pointed by Harrison et al. (2021), such as increasing magnitude of atmospheric CO_2
724 fluctuations, responses to warming, responses to atmospheric CO_2 , drought stress effects, etc.,
725 represent our knowledge gaps in ecosystem ecology. Experiments (Ainsworth and Long, 2004;



726 Crowther et al., 2016), observatory networks (Baldocchi et al., 2001), and remote sensing
727 (Duncanson et al., 2020), provide means to improve the modeling of terrestrial ecosystems.

728

729 **5.4 Model stability and complexity**

730 Ecosystem demographic processes (e.g., reproduction and mortality) are a source of high
731 sensitivity and uncertainty in BiomeE. In some environmental conditions, especially dry or cold
732 regions, the uniform parameters lead to high mortality or failure of reproduction, leading to high
733 instability of vegetation. To understand these issues, we developed a “single-cohort” version of
734 the model to aid in the diagnosis of issues in the full demographic version of the model. The
735 major issue we identified is the fact that the model formulation is based on functional processes
736 in highly-productive regions, whereas the model is applied globally and across much more
737 diverse environmental conditions (e.g., arid environments). The variables and parameters that
738 work well in highly-productive regions (e.g., initial seedling sizes, default leaf growth, minimum
739 allocation ratios, etc.) are often unsuitable in regions with higher environmental stress. And
740 although plants have evolved special features to deal with more extreme conditions (Lloret et al.,
741 2012; Reyer et al., 2013; Singh et al., 2020), these features have not yet been integrated into the
742 model.

743 There is a tendency in current DGVMs to use individual plant physiological trait changes
744 to represent community shifts. This approach is usually characterized as “parameter dynamics”
745 or “response functions” (Fisher and Koven, 2020) for reducing model processes and complexity.
746 Adding new processes to work around existing problems, instead of redesigning the fundamental
747 model processes, is common in model development. The approach is helpful for tracking model
748 development, undoing wrong additions, and improving model performance. However, work-



749 rounds often increase model complexity without concomitant improvements in model
750 predictions.

751 Generally, a model's usefulness is improved by transparent assumptions, a well-defined
752 model structure, and output that is testable against data (Famiglietti et al., 2021; Forster, 2017;
753 Hourdin et al., 2017). Data assimilation approaches improve model parameterization more
754 efficiently and effectively than manually tuning individual parameters (Williams et al., 2009;
755 MacBean et al., 2016; Wang et al., 2009) and allow for more detailed uncertainty analysis (Luo
756 et al., 2009; Weng et al., 2011; Weng and Luo, 2011; Xu et al., 2006; Dietze, 2014). It is
757 important to only include necessary assumptions in a model and to include them in ways that do
758 not compromise other processes or parameters. Modelers should try their best not to add poor-
759 understood processes if not necessary. Additionally, many specifications of model formulation
760 are based on the questions that a user is trying to answer in their research. We should not expect
761 to develop an all-encompassing model that fits all application scenarios. On the contrary,
762 maintaining model flexibility and transparency is critical for using this model as a tool to explore
763 specific science questions. In BiomeE, we have opted for what we consider the most
764 parsimonious and at the same time theoretically sound formulations of allometry, phenology, and
765 allocation dynamics to allow for computational efficiency in capturing vegetation growth and
766 ecological dynamics in the context of an ESM.

767

768 **5.5 Legacy limitations of code and model development conventions**

769 ModelE is a general circulation model, and vegetation in the model to date has been represented
770 with a simple set of static biophysics parameterizations to regulate exchanges of energy and
771 moisture between the land surface and the atmosphere (i.e., a big leaf model) (Hansen et al.,



772 2007; Schmidt et al., 2014; Kelley et al., 2020). To advance the functionality of the vegetation
773 and the land surface model within ModelE, increases in complexity must therefore be balanced
774 with the computational demands of the fully-coupled model. Time-consuming computations in
775 vegetation model can substantially reduce the speed of the whole model. In ModelE, the land
776 model, TerraE, is used to calculate land surface (including vegetation) water and energy fluxes
777 and soil water dynamics based on the characteristics of vegetation derived from the vegetation
778 model (e.g., canopy conductance, wetness, etc.) at the grid scale. It does not calculate each
779 cohort's transpiration and water uptake.

780 In our vegetation model, the water limitation of stomatal conductance is calculated as a
781 function of soil water stress index and root vertical distribution, instead of the direct plant root
782 water supply (plant hydraulics). This setting works well for the big leaf model (one canopy at
783 one grid). However, when multiple cohorts of plants are represented in the model, it is unable to
784 represent water competition and differentiate the contribution of each single cohort's
785 contribution to the total transpiration. A structural change is required to solve this problem by
786 calculating transpiration from the bottom up (i.e., from cohort up to grid cell).

787 The legacy of model coding structure and the history of model development can greatly
788 affect the functions and the selection of model formulations (Alexander and Easterbrook, 2015).
789 When incorporating new processes, especially a new vegetation dynamic model, we must
790 balance the stability requirement of the parent model and the risks of the model crashing. As
791 shown in the comparison with the single cohort model (Fig. 11), the full demography setting has
792 many potential failing points in regeneration in more extreme environmental conditions.

793

794 **6 Conclusions**



795 We developed a new demographic vegetation model to improve the representation of terrestrial
796 vegetation dynamics and ecosystem biogeochemical cycles in the NASA Goddard Institute of
797 Space Studies' coupled Earth system model, ModelE. This model includes the processes of plant
798 growth, mortality, reproduction, vegetation structural dynamics, and soil carbon and nitrogen
799 cycling. To scale this model globally, we added a new set of plant functional types to represent
800 global vegetation functional diversity and introduced new phenology algorithms to deal with the
801 seasonality of temperature and soil water availability. Competition for light and soil resources is
802 individual-based, which makes the modeling of eco-evolutionary optimality possible. This model
803 predicts the dynamics of vegetation and soil biogeochemistry including leaf area index,
804 vegetation structure (e.g., height, tree density, size distribution, crown organization), and
805 ecosystem carbon and nitrogen storage and fluxes. This model will enable ModelE to simulate
806 long-term biogeophysical and biogeochemical feedbacks between the climate system and land
807 ecosystems at decadal to century temporal scales. It will also allow for the prediction of transient
808 vegetation dynamics and eco-evolutionary community assemblage in response to future climate
809 changes based on the fundamental ecological principles.

810

811

812 **Code and data availability**

813 The model codes have been coupled with NASA GISS ModelE and will be released with
814 ModelE codes (<https://www.giss.nasa.gov/tools/modelE/>). We put the relevant code files at
815 GitHub for review proposes (<https://github.com/wengensheng/ModelE-BiomeE>). The simulated
816 data are stored at NASA supercomputer discover. We will make them publicly available at the
817 acceptance of this paper.



818

819 **Author contributions**

820 EW coded the model and performed test runs and data analysis. EW and BIC wrote the first draft
821 of the manuscript. BIC, MJP, SSM, NYK, and EW designed the functional coupling with
822 ModelE and the land module. NYK, IA, RS, and MK contributed to input data, the IO structure
823 and the coupling between BiomeE and Ent. KW, RD, CE, and SWP contributed to conceptual
824 model development and PFT design. All co-authors contributed to writing or improving the
825 manuscript.

826

827 **Competing interests**

828 The authors declare that they have no conflict of interest.

829

830 **Acknowledgements**

831 This work was supported by NASA Modeling, Analysis, and Prediction (MAP) Program (GISS
832 Model development and NNH20ZDA001N-MAP). Computing resources for the model runs
833 were provided by the NASA High-End Computing (HEC) Program through the NASA Center
834 for Climate Simulation (NCCS) at Goddard Space Flight Center. We thank Dr. Pierre Gentine of
835 Department of Earth and Environmental Engineering, Columbia University, for his help in GPP
836 data and model validation.



837 **Reference**

- 838 Aakala, T., Fraver, S., Palik, B. J., and D'Amato, A. W.: Spatially random mortality in old-
839 growth red pine forests of northern Minnesota, 42, 899–907, <https://doi.org/10.1139/x2012-044>,
840 2012.
- 841 Abramoff, R. Z. and Finzi, A. C.: Are above- and below-ground phenology in sync?, 205, 1054–
842 1061, <https://doi.org/10.1111/nph.13111>, 2015.
- 843 Ainsworth, E. A. and Long, S. P.: What have we learned from 15 years of free-air CO₂
844 enrichment (FACE)? A meta-analytic review of the responses of photosynthesis, canopy
845 properties and plant production to rising CO₂: Tansley review, 165, 351–372,
846 <https://doi.org/10.1111/j.1469-8137.2004.01224.x>, 2004.
- 847 Aleixo, I., Norris, D., Hemerik, L., Barbosa, A., Prata, E., Costa, F., and Poorter, L.: Amazonian
848 rainforest tree mortality driven by climate and functional traits, 9, 384–388,
849 <https://doi.org/10.1038/s41558-019-0458-0>, 2019.
- 850 Alemohammad, S. H., Fang, B., Konings, A. G., Aires, F., Green, J. K., Kolassa, J., Miralles, D.,
851 Prigent, C., and Gentine, P.: Water, Energy, and Carbon with Artificial Neural Networks
852 (WECANN): a statistically based estimate of global surface turbulent fluxes and gross primary
853 productivity using solar-induced fluorescence, 14, 4101–4124, <https://doi.org/10.5194/bg-14-4101-2017>, 2017.
- 855 Alexander, K. and Easterbrook, S. M.: The software architecture of climate models: a graphical
856 comparison of CMIP5 and EMICAR5 configurations, 8, 1221–1232,
857 <https://doi.org/10.5194/gmd-8-1221-2015>, 2015.
- 858 Allen, C. D., Macalady, A. K., Chenchouni, H., Bachelet, D., McDowell, N., Vennetier, M.,
859 Kitzberger, T., Rigling, A., Breshears, D. D., Hogg, E. H. (Ted), Gonzalez, P., Fensham, R.,
860 Zhang, Z., Castro, J., Demidova, N., Lim, J.-H., Allard, G., Running, S. W., Semerci, A., and
861 Cobb, N.: A global overview of drought and heat-induced tree mortality reveals emerging
862 climate change risks for forests, 259, 660–684, <https://doi.org/10.1016/j.foreco.2009.09.001>,
863 2010.
- 864 Anderegg, W. R. L., Kane, J. M., and Anderegg, L. D. L.: Consequences of widespread tree
865 mortality triggered by drought and temperature stress, 3, 30–36,
866 <https://doi.org/10.1038/nclimate1635>, 2012.
- 867 Anten, N. P.: Evolutionarily stable leaf area production in plant populations, 217, 15–32, 2002.
- 868 Argles, A. P. K., Moore, J. R., Huntingford, C., Wiltshire, A. J., Harper, A. B., Jones, C. D., and
869 Cox, P. M.: Robust Ecosystem Demography (RED version 1.0): a parsimonious approach to
870 modelling vegetation dynamics in Earth system models, 13, 4067–4089,
871 <https://doi.org/10.5194/gmd-13-4067-2020>, 2020.



- 872 Arora, V. K. and Boer, G. J.: A parameterization of leaf phenology for the terrestrial ecosystem
873 component of climate models, 11, 39–59, <https://doi.org/10.1111/j.1365-2486.2004.00890.x>,
874 2005.
- 875 Arora, V. K., Katavouta, A., Williams, R. G., Jones, C. D., Brovkin, V., Friedlingstein, P.,
876 Schwinger, J., Bopp, L., Boucher, O., Cadule, P., Chamberlain, M. A., Christian, J. R., Delire,
877 C., Fisher, R. A., Hajima, T., Ilyina, T., Joetzjer, E., Kawamiya, M., Koven, C. D., Krasting, J.
878 P., Law, R. M., Lawrence, D. M., Lenton, A., Lindsay, K., Pongratz, J., Raddatz, T., Séférian,
879 R., Tachiiri, K., Tjiputra, J. F., Wiltshire, A., Wu, T., and Ziehn, T.: Carbon–concentration and
880 carbon–climate feedbacks in CMIP6 models and their comparison to CMIP5 models, 17, 4173–
881 4222, <https://doi.org/10.5194/bg-17-4173-2020>, 2020.
- 882 Avissar, R. and Werth, D.: Global Hydroclimatological Teleconnections Resulting from Tropical
883 Deforestation, *J. Hydrometeor.*, 6, 134–145, <https://doi.org/10.1175/JHM406.1>, 2005.
- 884 Baldocchi, D., Falge, E., Gu, L., Olson, R., Hollinger, D., Running, S., Anthoni, P., Bernhofer,
885 C., Davis, K., Evans, R., Fuentes, J., Goldstein, A., Katul, G., Law, B., Lee, X., Malhi, Y.,
886 Meyers, T., Munger, W., Oechel, W., Paw U, K. T., Pilegaard, K., Schmid, H. P., Valentini, R.,
887 Verma, S., Vesala, T., Wilson, K., and Wofsy, S.: FLUXNET: A New Tool to Study the
888 Temporal and Spatial Variability of Ecosystem-Scale Carbon Dioxide, Water Vapor, and Energy
889 Flux Densities, *Bull. Amer. Meteor. Soc.*, 82, 2415–2434, [https://doi.org/10.1175/1520-0477\(2001\)082<2415:FANTTS>2.3.CO;2](https://doi.org/10.1175/1520-0477(2001)082<2415:FANTTS>2.3.CO;2), 2001.
- 891 Bonan, G. B., Lawrence, P. J., Oleson, K. W., Levis, S., Jung, M., Reichstein, M., Lawrence, D.
892 M., and Swenson, S. C.: Improving canopy processes in the Community Land Model version 4
893 (CLM4) using global flux fields empirically inferred from FLUXNET data, 116,
894 <https://doi.org/10.1029/2010JG001593>, 2011.
- 895 Brando, P. M., Paolucci, L., Ummenhofer, C. C., Ordway, E. M., Hartmann, H., Cattau, M. E.,
896 Rattis, L., Medjibe, V., Coe, M. T., and Balch, J.: Droughts, Wildfires, and Forest Carbon
897 Cycling: A Pantropical Synthesis, *Annu. Rev. Earth Planet. Sci.*, 47, 555–581,
898 <https://doi.org/10.1146/annurev-earth-082517-010235>, 2019.
- 899 Brodrribb, T. J., Powers, J., Cochard, H., and Choat, B.: Hanging by a thread? Forests and
900 drought, 368, 261–266, <https://doi.org/10.1126/science.aat7631>, 2020.
- 901 Caldararu, S., Purves, D. W., and Palmer, P. I.: Phenology as a strategy for carbon optimality: a
902 global model, 11, 763–778, <https://doi.org/10.5194/bg-11-763-2014>, 2014.
- 903 Chave, J., Coomes, D., Jansen, S., Lewis, S. L., Swenson, N. G., and Zanne, A. E.: Towards a
904 worldwide wood economics spectrum, 12, 351–366, <https://doi.org/10.1111/j.1461-0248.2009.01285.x>, 2009.
- 906 Chen, M., Melaas, E. K., Gray, J. M., Friedl, M. A., and Richardson, A. D.: A new seasonal-
907 deciduous spring phenology submodel in the Community Land Model 4.5: impacts on carbon
908 and water cycling under future climate scenarios, 22, 3675–3688,
909 <https://doi.org/10.1111/gcb.13326>, 2016.



- 910 Choat, B., Jansen, S., Brodribb, T. J., Cochard, H., Delzon, S., Bhaskar, R., Bucci, S. J., Feild, T.
911 S., Gleason, S. M., Hacke, U. G., Jacobsen, A. L., Lens, F., Maherali, H., Martínez-Vilalta, J.,
912 Mayr, S., Mencuccini, M., Mitchell, P. J., Nardini, A., Pittermann, J., Pratt, R. B., Sperry, J. S.,
913 Westoby, M., Wright, I. J., and Zanne, A. E.: Global convergence in the vulnerability of forests
914 to drought, <https://doi.org/10.1038/nature11688>, 2012.
- 915 Chuine, I.: Why does phenology drive species distribution?, 365, 3149–3160,
916 <https://doi.org/10.1098/rstb.2010.0142>, 2010.
- 917 Clark, J. S., Iverson, L., Woodall, C. W., Allen, C. D., Bell, D. M., Bragg, D. C., D’Amato, A.
918 W., Davis, F. W., Hersh, M. H., Ibanez, I., Jackson, S. T., Matthews, S., Pederson, N., Peters,
919 M., Schwartz, M. W., Waring, K. M., and Zimmermann, N. E.: The impacts of increasing
920 drought on forest dynamics, structure, and biodiversity in the United States, 22, 2329–2352,
921 <https://doi.org/10.1111/gcb.13160>, 2016.
- 922 Crowther, T. W., Todd-Brown, K. E. O., Rowe, C. W., Wieder, W. R., Carey, J. C., Machmuller,
923 M. B., Snoek, B. L., Fang, S., Zhou, G., Allison, S. D., Blair, J. M., Bridgham, S. D., Burton, A.
924 J., Carrillo, Y., Reich, P. B., Clark, J. S., Classen, A. T., Dijkstra, F. A., Elberling, B., Emmett,
925 B. A., Estiarte, M., Frey, S. D., Guo, J., Harte, J., Jiang, L., Johnson, B. R., Kröel-Dulay, G.,
926 Larsen, K. S., Laudon, H., Lavalley, J. M., Luo, Y., Lupascu, M., Ma, L. N., Marhan, S.,
927 Michelsen, A., Mohan, J., Niu, S., Pendall, E., Peñuelas, J., Pfeifer-Meister, L., Poll, C., Reinsch,
928 S., Reynolds, L. L., Schmidt, I. K., Sistla, S., Sokol, N. W., Templer, P. H., Treseder, K. K.,
929 Welker, J. M., and Bradford, M. A.: Quantifying global soil carbon losses in response to
930 warming, 540, 104–108, <https://doi.org/10.1038/nature20150>, 2016.
- 931 Dahlin, K. M., Fisher, R. A., and Lawrence, P. J.: Environmental drivers of drought deciduous
932 phenology in the Community Land Model, 12, 5061–5074, [https://doi.org/10.5194/bg-12-5061-](https://doi.org/10.5194/bg-12-5061-2015)
933 2015, 2015.
- 934 De Kauwe, M. G., Zhou, S.-X., Medlyn, B. E., Pitman, A. J., Wang, Y.-P., Duursma, R. A., and
935 Prentice, I. C.: Do land surface models need to include differential plant species responses to
936 drought? Examining model predictions across a mesic-xeric gradient in Europe, 12, 7503–7518,
937 <https://doi.org/10.5194/bg-12-7503-2015>, 2015.
- 938 Dieckmann, U., Brannstrom, A., HilleRisLambes, R., and Ito, H. C.: The Adaptive Dynamics of
939 Community Structure, in: *Mathematics for Ecology and Environmental Sciences*, edited by:
940 Takeuchi, Yasuhiro, Iwasa, Yoh, and Sato, Kazunori, Springer, 145–177, 2007.
- 941 Dietze, M. C.: Gaps in knowledge and data driving uncertainty in models of photosynthesis, 119,
942 3–14, <https://doi.org/10.1007/s11120-013-9836-z>, 2014.
- 943 Duncanson, L., Neuenschwander, A., Hancock, S., Thomas, N., Fatoyinbo, T., Simard, M.,
944 Silva, C. A., Armston, J., Luthcke, S. B., Hofton, M., Kellner, J. R., and Dubayah, R.: Biomass
945 estimation from simulated GEDI, ICESat-2 and NISAR across environmental gradients in
946 Sonoma County, California, *Remote Sensing of Environment*, 242, 111779,
947 <https://doi.org/10.1016/j.rse.2020.111779>, 2020.



- 948 Dybzinski, R., Farrior, C. E., and Pacala, S. W.: Increased forest carbon storage with increased
949 atmospheric CO₂ despite nitrogen limitation: a game-theoretic allocation model for trees in
950 competition for nitrogen and light, 21, 1182–1196, <https://doi.org/10.1111/gcb.12783>, 2015.
- 951 Falster, D. and Westoby, M.: Plant height and evolutionary games, 18, 337–343,
952 [https://doi.org/10.1016/S0169-5347\(03\)00061-2](https://doi.org/10.1016/S0169-5347(03)00061-2), 2003.
- 953 Falster, D. S., Braennstroem, A., Westoby, M., and Dieckmann, U.: Multitrait successional forest
954 dynamics enable diverse competitive coexistence, 114, E2719–E2728,
955 <https://doi.org/10.1073/pnas.1610206114>, 2017.
- 956 Famiglietti, C. A., Smallman, T. L., Levine, P. A., Flack-Prain, S., Quetin, G. R., Meyer, V.,
957 Parazoo, N. C., Stettz, S. G., Yang, Y., Bonal, D., Bloom, A. A., Williams, M., and Konings, A.
958 G.: Optimal model complexity for terrestrial carbon cycle prediction, 18, 2727–2754,
959 <https://doi.org/10.5194/bg-18-2727-2021>, 2021.
- 960 Farquhar, G. D., Caemmerer, S. V., and Berry, J. A.: A biochemical model of photosynthetic
961 CO₂ assimilation in leaves of C₃ species, 149, 78–90, <https://doi.org/10.1007/BF00386231>,
962 1980.
- 963 Farrior, C. E., Dybzinski, R., Levin, S. A., and Pacala, S. W.: Competition for Water and Light
964 in Closed-Canopy Forests: A Tractable Model of Carbon Allocation with Implications for
965 Carbon Sinks, 181, 314–330, <https://doi.org/10.1086/669153>, 2013.
- 966 Fisher, R. A. and Koven, C. D.: Perspectives on the Future of Land Surface Models and the
967 Challenges of Representing Complex Terrestrial Systems, 12, e2018MS001453,
968 <https://doi.org/10.1029/2018MS001453>, 2020.
- 969 Fisher, R. A., Muszala, S., Versteinstein, M., Lawrence, P., Xu, C., McDowell, N. G., Knox, R.
970 G., Koven, C., Holm, J., Rogers, B. M., Spessa, A., Lawrence, D., and Bonan, G.: Taking off the
971 training wheels: the properties of a dynamic vegetation model without climate envelopes,
972 CLM4.5(ED), 8, 3593–3619, <https://doi.org/10.5194/gmd-8-3593-2015>, 2015.
- 973 von Foerster, H.: Some remarks on changing populations, in: The kinetics of cellular proliferatio,
974 edited by: Stohlman, F., Grune and Stratton, New York, 382–407, 1959.
- 975 Forster, P.: Half a century of robust climate models, 545, 296–297,
976 <https://doi.org/10.1038/545296a>, 2017.
- 977 Franklin, O., Harrison, S. P., Dewar, R., Farrior, C. E., Brännström, Å., Dieckmann, U., Pietsch,
978 S., Falster, D., Cramer, W., Loreau, M., Wang, H., Mäkelä, A., Rebel, K. T., Meron, E.,
979 Schymanski, S. J., Rovenskaya, E., Stocker, B. D., Zaehle, S., Manzoni, S., van Oijen, M.,
980 Wright, I. J., Ciais, P., van Bodegom, P. M., Peñuelas, J., Hofhansl, F., Terrer, C.,
981 Soudzilovskaia, N. A., Midgley, G., and Prentice, I. C.: Organizing principles for vegetation
982 dynamics, 1–10, <https://doi.org/10.1038/s41477-020-0655-x>, 2020.



- 983 Friedl, M. A., Sulla-Menashe, D., Tan, B., Schneider, A., Ramankutty, N., Sibley, A., and
984 Huang, X.: MODIS Collection 5 global land cover: Algorithm refinements and characterization
985 of new datasets, 114, 168–182, <https://doi.org/10.1016/j.rse.2009.08.016>, 2010.
- 986 Friedlingstein, P., Meinshausen, M., Arora, V. K., Jones, C. D., Anav, A., Liddicoat, S. K., and
987 Knutti, R.: Uncertainties in CMIP5 Climate Projections due to Carbon Cycle Feedbacks, 27,
988 511–526, <https://doi.org/10.1175/JCLI-D-12-00579.1>, 2014.
- 989 Friend, A. D., Stevens, A. K., Knox, R. G., and Cannell, M. G. R.: A process-based, terrestrial
990 biosphere model of ecosystem dynamics (Hybrid v3.0), *Ecological Modelling*, 95, 249–287,
991 [https://doi.org/10.1016/S0304-3800\(96\)00034-8](https://doi.org/10.1016/S0304-3800(96)00034-8), 1997.
- 992 Garcia, E. S., Swann, A. L. S., Villegas, J. C., Breshears, D. D., Law, D. J., Saleska, S. R., and
993 Stark, S. C.: Synergistic Ecoclimate Teleconnections from Forest Loss in Different Regions
994 Structure Global Ecological Responses, *PLoS One*, 11,
995 <https://doi.org/10.1371/journal.pone.0165042>, 2016.
- 996 Gleason, K. E., Bradford, J. B., Bottero, A., D’Amato, A. W., Fraver, S., Palik, B. J., Battaglia,
997 M. A., Iverson, L., Kenefic, L., and Kern, C. C.: Competition amplifies drought stress in forests
998 across broad climatic and compositional gradients, 8, e01849, <https://doi.org/10.1002/ecs2.1849>,
999 2017.
- 1000 Green, J. K., Konings, A. G., Alemohammad, S. H., Berry, J., Entekhabi, D., Kolassa, J., Lee, J.-
1001 E., and Gentine, P.: Regionally strong feedbacks between the atmosphere and terrestrial
1002 biosphere, *Nature Geosci*, 10, 410–414, <https://doi.org/10.1038/ngeo2957>, 2017.
- 1003 Hansen, J., Sato, M., Ruedy, R., Kharecha, P., Lacis, A., Miller, R., Nazarenko, L., Lo, K.,
1004 Schmidt, G. A., Russell, G., Aleinov, I., Bauer, S., Baum, E., Cairns, B., Canuto, V., Chandler,
1005 M., Cheng, Y., Cohen, A., Del Genio, A., Faluvegi, G., Fleming, E., Friend, A., Hall, T.,
1006 Jackman, C., Jonas, J., Kelley, M., Kiang, N. Y., Koch, D., Labow, G., Lerner, J., Menon, S.,
1007 Novakov, T., Oinas, V., Perlwitz, Ja., Perlwitz, Ju., Rind, D., Romanou, A., Schmunk, R.,
1008 Shindell, D., Stone, P., Sun, S., Streets, D., Tausnev, N., Thresher, D., Unger, N., Yao, M., and
1009 Zhang, S.: Climate simulations for 1880–2003 with GISS modelE, 29, 661–696,
1010 <https://doi.org/10.1007/s00382-007-0255-8>, 2007.
- 1011 Harper, A. B., Williams, K. E., McGuire, P. C., Duran Rojas, M. C., Hemming, D., Verhoef, A.,
1012 Huntingford, C., Rowland, L., Marthews, T., Breder Eller, C., Mathison, C., Nobrega, R. L. B.,
1013 Gedney, N., Vidale, P. L., Otu-Larbi, F., Pandey, D., Garrigues, S., Wright, A., Slevin, D., De
1014 Kauwe, M. G., Blyth, E., Ardö, J., Black, A., Bonal, D., Buchmann, N., Burban, B., Fuchs, K.,
1015 de Grandcourt, A., Mammarella, I., Merbold, L., Montagnani, L., Nouvellon, Y., Restrepo-
1016 Coupe, N., and Wohlfahrt, G.: Improvement of modeling plant responses to low soil moisture in
1017 JULESv4.9 and evaluation against flux tower measurements, 14, 3269–3294,
1018 <https://doi.org/10.5194/gmd-14-3269-2021>, 2021.
- 1019 Harrison, S. P., Cramer, W., Franklin, O., Prentice, I. C., Wang, H., Brännström, Å., de Boer, H.,
1020 Dieckmann, U., Joshi, J., Keenan, T. F., Lavergne, A., Manzoni, S., Mengoli, G., Morfopoulos,
1021 C., Peñuelas, J., Pietsch, S., Rebel, K. T., Ryu, Y., Smith, N. G., Stocker, B. D., and Wright, I. J.:



- 1022 Eco-evolutionary optimality as a means to improve vegetation and land-surface models, 231,
1023 2125–2141, <https://doi.org/10.1111/nph.17558>, 2021.
- 1024 Hengeveld, G. M., Gunia, K., Didion, M., Zudin, S., Clerkx, A. P. P. M., and Schelhaas, M. J.:
1025 Global 1-degree Maps of Forest Area, Carbon Stocks, and Biomass, 1950-2010,
1026 <https://doi.org/10.3334/ORNLDAAAC/1296>, 2015.
- 1027 Hikosaka, K. and Anten, N. P. R.: An evolutionary game of leaf dynamics and its consequences
1028 for canopy structure, 26, 1024–1032, <https://doi.org/10.1111/j.1365-2435.2012.02042.x>, 2012.
- 1029 Hourdin, F., Mauritsen, T., Gettelman, A., Golaz, J.-C., Balaji, V., Duan, Q., Folini, D., Ji, D.,
1030 Klocke, D., Qian, Y., Rauser, F., Rio, C., Tomassini, L., Watanabe, M., and Williamson, D.: The
1031 Art and Science of Climate Model Tuning, 98, 589–602, <https://doi.org/10.1175/BAMS-D-15-00135.1>, 2017.
- 1033 Huang, M., Piao, S., Sun, Y., Ciais, P., Cheng, L., Mao, J., Poulter, B., Shi, X., Zeng, Z., and
1034 Wang, Y.: Change in terrestrial ecosystem water-use efficiency over the last three decades, 21,
1035 2366–2378, <https://doi.org/10.1111/gcb.12873>, 2015.
- 1036 Huntzinger, D. N., Post, W. M., Wei, Y., Michalak, A. M., West, T. O., Jacobson, A. R., Baker,
1037 I. T., Chen, J. M., Davis, K. J., Hayes, D. J., Hoffman, F. M., Jain, A. K., Liu, S., McGuire, A.
1038 D., Neilson, R. P., Potter, C., Poulter, B., Price, D., Raczka, B. M., Tian, H. Q., Thornton, P.,
1039 Tomelleri, E., Viovy, N., Xiao, J., Yuan, W., Zeng, N., Zhao, M., and Cook, R.: North American
1040 Carbon Program (NACP) regional interim synthesis: Terrestrial biospheric model
1041 intercomparison, 232, 144–157, <https://doi.org/10.1016/j.ecolmodel.2012.02.004>, 2012.
- 1042 Ito, G., Romanou, A., Kiang, N. Y., Faluvegi, G., Aleinov, I., Ruedy, R., Russell, G., Lerner, P.,
1043 Kelley, M., and Lo, K.: Global Carbon Cycle and Climate Feedbacks in the NASA GISS
1044 ModelE2.1, 12, e2019MS002030, <https://doi.org/10.1029/2019MS002030>, 2020.
- 1045 Keenan, T. F., Hollinger, D. Y., Bohrer, G., Dragoni, D., Munger, J. W., Schmid, H. P., and
1046 Richardson, A. D.: Increase in forest water-use efficiency as atmospheric carbon dioxide
1047 concentrations rise, 499, 324–327, <https://doi.org/10.1038/nature12291>, 2013.
- 1048 Kelley, M., Schmidt, G. A., Nazarenko, L. S., Bauer, S. E., Ruedy, R., Russell, G. L., Ackerman,
1049 A. S., Aleinov, I., Bauer, M., Bleck, R., Canuto, V., Cesana, G., Cheng, Y., Clune, T. L., Cook,
1050 B. I., Cruz, C. A., Del Genio, A. D., Elsaesser, G. S., Faluvegi, G., Kiang, N. Y., Kim, D., Lacis,
1051 A. A., LeBoissetier, A., LeGrande, A. N., Lo, K. K., Marshall, J., Matthews, E. E., McDermid,
1052 S., Mezuman, K., Miller, R. L., Murray, L. T., Oinas, V., Orbe, C., García-Pando, C. P.,
1053 Perlwitz, J. P., Puma, M. J., Rind, D., Romanou, A., Shindell, D. T., Sun, S., Tausnev, N.,
1054 Tsigaridis, K., Tselioudis, G., Weng, E., Wu, J., and Yao, M.-S.: GISS-E2.1: Configurations and
1055 Climatology, *Journal of Advances in Modeling Earth Systems*, 12, e2019MS002025,
1056 <https://doi.org/10.1029/2019MS002025>, 2020.
- 1057 Kim, Y., Moorcroft, P. R., Aleinov, I., Puma, M. J., and Kiang, N. Y.: Variability of phenology
1058 and fluxes of water and carbon with observed and simulated soil moisture in the Ent Terrestrial
1059 Biosphere Model (Ent TBM version 1.0.1.0.0), 8, 3837–3865, <https://doi.org/10.5194/gmd-8-3837-2015>, 2015.



- 1061 Kyker-Snowman, E., Lombardozzi, D. L., Bonan, G. B., Cheng, S. J., Dukes, J. S., Frey, S. D.,
1062 Jacobs, E. M., McNellis, R., Rady, J. M., Smith, N. G., Thomas, R. Q., Wieder, W. R., and
1063 Grandy, A. S.: Increasing the spatial and temporal impact of ecological research: A roadmap for
1064 integrating a novel terrestrial process into an Earth system model, 28, 665–684,
1065 <https://doi.org/10.1111/gcb.15894>, 2022.
- 1066 Liu, H., Gleason, S. M., Hao, G., Hua, L., He, P., Goldstein, G., and Ye, Q.: Hydraulic traits are
1067 coordinated with maximum plant height at the global scale, 5, eaav1332,
1068 <https://doi.org/10.1126/sciadv.aav1332>, 2019.
- 1069 Lloret, F., Escudero, A., Iriondo, J. M., Martínez-Vilalta, J., and Valladares, F.: Extreme climatic
1070 events and vegetation: the role of stabilizing processes, 18, 797–805,
1071 <https://doi.org/10.1111/j.1365-2486.2011.02624.x>, 2012.
- 1072 Lu, M. and Hedin, L. O.: Global plant–symbiont organization and emergence of biogeochemical
1073 cycles resolved by evolution-based trait modelling, *Nat Ecol Evol*, 3, 239–250,
1074 <https://doi.org/10.1038/s41559-018-0759-0>, 2019.
- 1075 Lu, R., Qiao, Y., Wang, J., Zhu, C., Cui, E., Xu, X., He, Y., Zhao, Z., Du, Y., Yan, L., Shen, G.,
1076 Yang, Q., Wang, X., and Xia, J.: The U-shaped pattern of size-dependent mortality and its
1077 correlated factors in a subtropical monsoon evergreen forest, 109, 2421–2433,
1078 <https://doi.org/10.1111/1365-2745.13652>, 2021.
- 1079 Luo, Y., Weng, E., Wu, X., Gao, C., Zhou, X., and Zhang, L.: Parameter identifiability,
1080 constraint, and equifinality in data assimilation with ecosystem models, 19, 571–574,
1081 <https://doi.org/10.1890/08-0561.1>, 2009.
- 1082 MacBean, N., Peylin, P., Chevallier, F., Scholze, M., and Schuermann, G.: Consistent
1083 assimilation of multiple data streams in a carbon cycle data assimilation system, 9, 3569–3588,
1084 <https://doi.org/10.5194/gmd-9-3569-2016>, 2016.
- 1085 Manzoni, S., Trofymow, J. A., Jackson, R. B., and Porporato, A.: Stoichiometric controls on
1086 carbon, nitrogen, and phosphorus dynamics in decomposing litter, 80, 89–106, 2010.
- 1087 Manzoni, S., Vico, G., Thompson, S., Beyer, F., and Weih, M.: Contrasting leaf phenological
1088 strategies optimize carbon gain under droughts of different duration, *Advances in Water*
1089 *Resources*, 84, 37–51, <https://doi.org/10.1016/j.advwatres.2015.08.001>, 2015.
- 1090 McDowell, N. G.: Mechanisms Linking Drought, Hydraulics, Carbon Metabolism, and
1091 Vegetation Mortality, 155, 1051–1059, <https://doi.org/10.1104/pp.110.170704>, 2011.
- 1092 McDowell, N. G., Allen, C. D., Anderson-Teixeira, K., Aukema, B. H., Bond-Lamberty, B.,
1093 Chini, L., Clark, J. S., Dietze, M., Grossiord, C., Hanbury-Brown, A., Hurtt, G. C., Jackson, R.
1094 B., Johnson, D. J., Kueppers, L., Lichstein, J. W., Ogle, K., Poulter, B., Pugh, T. A. M., Seidl,
1095 R., Turner, M. G., Uriarte, M., Walker, A. P., and Xu, C.: Pervasive shifts in forest dynamics in a
1096 changing world, 368, <https://doi.org/10.1126/science.aaz9463>, 2020.



- 1097 McNickle, G. G., Gonzalez-Meler, M. A., Lynch, D. J., Baltzer, J. L., and Brown, J. S.: The
1098 world's biomes and primary production as a triple tragedy of the commons foraging game played
1099 among plants, 283, 20161993, <https://doi.org/10.1098/rspb.2016.1993>, 2016.
- 1100 Meir, P., Cox, P., and Grace, J.: The influence of terrestrial ecosystems on climate, Trends in
1101 Ecology & Evolution, 21, 254–260, <https://doi.org/10.1016/j.tree.2006.03.005>, 2006.
- 1102 van der Molen, M. K., Dolman, A. J., Ciais, P., Eglin, T., Gobron, N., Law, B. E., Meir, P.,
1103 Peters, W., Phillips, O. L., Reichstein, M., Chen, T., Dekker, S. C., Doubková, M., Friedl, M. A.,
1104 Jung, M., van den Hurk, B. J. J. M., de Jeu, R. A. M., Kruijt, B., Ohta, T., Rebel, K. T.,
1105 Plummer, S., Seneviratne, S. I., Sitch, S., Teuling, A. J., van der Werf, G. R., and Wang, G.:
1106 Drought and ecosystem carbon cycling, Agricultural and Forest Meteorology, 151, 765–773,
1107 <https://doi.org/10.1016/j.agrformet.2011.01.018>, 2011.
- 1108 Montané, F., Fox, A. M., Arellano, A. F., MacBean, N., Alexander, M. R., Dye, A., Bishop, D.
1109 A., Trouet, V., Babst, F., Hessl, A. E., Pederson, N., Blanken, P. D., Bohrer, G., Gough, C. M.,
1110 Litvak, M. E., Novick, K. A., Phillips, R. P., Wood, J. D., and Moore, D. J. P.: Evaluating the
1111 effect of alternative carbon allocation schemes in a land surface model (CLM4.5) on carbon
1112 fluxes, pools, and turnover in temperate forests, 10, 3499–3517, <https://doi.org/10.5194/gmd-10-3499-2017>, 2017.
- 1114 Niinemets, Ü. and Anten, N. P. R.: Packing the Photosynthetic Machinery: From Leaf to
1115 Canopy, in: Photosynthesis in silico: Understanding Complexity from Molecules to Ecosystems,
1116 edited by: Laisk, A., Nedbal, L., and Govindjee, Springer Netherlands, Dordrecht, 363–399,
1117 https://doi.org/10.1007/978-1-4020-9237-4_16, 2009.
- 1118 Niinemets, Ü., Keenan, T. F., and Hallik, L.: A worldwide analysis of within-canopy variations
1119 in leaf structural, chemical and physiological traits across plant functional types, 205, 973–993,
1120 <https://doi.org/10.1111/nph.13096>, 2015.
- 1121 Niklas, K.: Plant Height and the Properties of Some Herbaceous Stems, 75, 133–142,
1122 <https://doi.org/10.1006/anbo.1995.1004>, 1995.
- 1123 Nobre, C. A., Sellers, P. J., and Shukla, J.: Amazonian Deforestation and Regional Climate
1124 Change, J. Climate, 4, 957–988, [https://doi.org/10.1175/1520-0442\(1991\)004<0957:ADARCC>2.0.CO;2](https://doi.org/10.1175/1520-0442(1991)004<0957:ADARCC>2.0.CO;2), 1991.
- 1126 Oliveira, R. S., Eller, C. B., Barros, F. de V., Hirota, M., Brum, M., and Bittencourt, P.: Linking
1127 plant hydraulics and the fast–slow continuum to understand resilience to drought in tropical
1128 ecosystems, 230, 904–923, <https://doi.org/10.1111/nph.17266>, 2021.
- 1129 Osnas, J. L. D., Lichstein, J. W., Reich, P. B., and Pacala, S. W.: Global Leaf Trait
1130 Relationships: Mass, Area, and the Leaf Economics Spectrum, 340, 741–744,
1131 <https://doi.org/10.1126/science.1231574>, 2013.
- 1132 Pan, Y., Birdsey, R. A., Phillips, O. L., and Jackson, R. B.: The Structure, Distribution, and
1133 Biomass of the World's Forests, 44, 593–622, <https://doi.org/10.1146/annurev-ecolsys-110512-135914>, 2013.



- 1135 Pavlick, R., Drewry, D. T., Bohn, K., Reu, B., and Kleidon, A.: The Jena Diversity-Dynamic
1136 Global Vegetation Model (JeDi-DGVM): a diverse approach to representing terrestrial
1137 biogeography and biogeochemistry based on plant functional trade-offs, 10, 4137–4177,
1138 <https://doi.org/10.5194/bg-10-4137-2013>, 2013.
- 1139 Pielke, R. A., Sr., Avissar, RonI., Raupach, M., Dolman, A. J., Zeng, X., and Denning, A. S.:
1140 Interactions between the atmosphere and terrestrial ecosystems: influence on weather and
1141 climate, 4, 461–475, <https://doi.org/10.1046/j.1365-2486.1998.t01-1-00176.x>, 1998.
- 1142 Potter, C., Klooster, S., Myneni, R., Genovese, V., Tan, P., and Kumar, V.: Continental-scale
1143 comparisons of terrestrial carbon sinks estimated from satellite data and ecosystem modeling
1144 1982–1998, 39, 201–213, <https://doi.org/10.1016/j.gloplacha.2003.07.001>, 2003.
- 1145 Potter, C. S., Randerson, J. T., Field, C. B., Matson, P. A., Vitousek, P. M., Mooney, H. A., and
1146 Klooster, S. A.: Terrestrial ecosystem production: A process model based on global satellite and
1147 surface data, 7, 811–841, <https://doi.org/10.1029/93GB02725>, 1993.
- 1148 Powell, T. L., Galbraith, D. R., Christoffersen, B. O., Harper, A., Imbuzeiro, H. M. A., Rowland,
1149 L., Almeida, S., Brando, P. M., da Costa, A. C. L., Costa, M. H., Levine, N. M., Malhi, Y.,
1150 Saleska, S. R., Sotta, E., Williams, M., Meir, P., and Moorcroft, P. R.: Confronting model
1151 predictions of carbon fluxes with measurements of Amazon forests subjected to experimental
1152 drought, 200, 350–365, <https://doi.org/10.1111/nph.12390>, 2013.
- 1153 Prentice, I. C., Cramer, W., Harrison, S. P., LEEMANS, R., Monserud, R. A., and Solomon, A.
1154 M.: A global biome model based on plant physiology and dominance, soil properties and
1155 climate, 19, 117–134, <https://doi.org/10.2307/2845499>, 1992.
- 1156 Prentice, I. C., Bondeau, A., Cramer, W., Harrison, S. P., Hickler, T., Lucht, W., Sitch, S., Smith,
1157 B., and Sykes, M. T.: Dynamic Global Vegetation Modeling: Quantifying Terrestrial Ecosystem
1158 Responses to Large-Scale Environmental Change, in: Terrestrial Ecosystems in a Changing
1159 World, edited by: Canadell, J. G., Pataki, D. E., and Pitelka, L. F., Springer Berlin Heidelberg,
1160 Berlin, Heidelberg, 175–192, https://doi.org/10.1007/978-3-540-32730-1_15, 2007.
- 1161 Prentice, I. C., Dong, N., Gleason, S. M., Maire, V., and Wright, I. J.: Balancing the costs of
1162 carbon gain and water transport: testing a new theoretical framework for plant functional
1163 ecology, 17, 82–91, <https://doi.org/10.1111/ele.12211>, 2014.
- 1164 Purves, D. and Pacala, S.: Predictive models of forest dynamics, 320, 1452–1453,
1165 <https://doi.org/10.1126/science.1155359>, 2008.
- 1166 Purves, D. W., Lichstein, J. W., Strigul, N., and Pacala, S. W.: Predicting and understanding
1167 forest dynamics using a simple tractable model, 105, 17018–17022,
1168 <https://doi.org/10.1073/pnas.0807754105>, 2008.
- 1169 Randerson, J., Thompson, M., Conway, T., Fung, I., and Field, C.: The contribution of terrestrial
1170 sources and sinks to trends in the seasonal cycle of atmospheric carbon dioxide, 11, 535–560,
1171 <https://doi.org/10.1029/97GB02268>, 1997.



- 1172 Reich, P. B.: The world-wide ‘fast–slow’ plant economics spectrum: a traits manifesto, 102,
1173 275–301, <https://doi.org/10.1111/1365-2745.12211>, 2014.
- 1174 Reyer, C. P. O., Leuzinger, S., Rammig, A., Wolf, A., Bartholomeus, R. P., Bonfante, A., de
1175 Lorenzi, F., Dury, M., Gloning, P., Abou Jaoudé, R., Klein, T., Kuster, T. M., Martins, M.,
1176 Niedrist, G., Riccardi, M., Wohlfahrt, G., de Angelis, P., de Dato, G., François, L., Menzel, A.,
1177 and Pereira, M.: A plant’s perspective of extremes: terrestrial plant responses to changing
1178 climatic variability, 19, 75–89, <https://doi.org/10.1111/gcb.12023>, 2013.
- 1179 Rodriguez-Iturbe, I., Porporato, A., Ridolfi, L., Isham, V., and Coxi, D. R.: Probabilistic
1180 modelling of water balance at a point: the role of climate, soil and vegetation, 455, 3789–3805,
1181 <https://doi.org/10.1098/rspa.1999.0477>, 1999.
- 1182 Rosenzweig, C. and Abramopoulos, F.: Land-Surface Model Development for the GISS GCM,
1183 10, 2040–2054, [https://doi.org/10.1175/1520-0442\(1997\)010<2040:LSMDFT>2.0.CO;2](https://doi.org/10.1175/1520-0442(1997)010<2040:LSMDFT>2.0.CO;2), 1997.
- 1184 Scheiter, S., Langan, L., and Higgins, S. I.: Next-generation dynamic global vegetation models:
1185 learning from community ecology, 198, 957–969, <https://doi.org/10.1111/nph.12210>, 2013.
- 1186 Schmidt, G. A., Kelley, M., Nazarenko, L., Ruedy, R., Russell, G. L., Aleinov, I., Bauer, M.,
1187 Bauer, S. E., Bhat, M. K., Bleck, R., Canuto, V., Chen, Y.-H., Cheng, Y., Clune, T. L., Del
1188 Genio, A., de Fainchtein, R., Faluvegi, G., Hansen, J. E., Healy, R. J., Kiang, N. Y., Koch, D.,
1189 Lacis, A. A., LeGrande, A. N., Lerner, J., Lo, K. K., Matthews, E. E., Menon, S., Miller, R. L.,
1190 Oinas, V., Olosio, A. O., Perlwitz, J. P., Puma, M. J., Putman, W. M., Rind, D., Romanou, A.,
1191 Sato, M., Shindell, D. T., Sun, S., Syed, R. A., Tausnev, N., Tsigaridis, K., Unger, N.,
1192 Voulgarakis, A., Yao, M.-S., and Zhang, J.: Configuration and assessment of the GISS ModelE2
1193 contributions to the CMIP5 archive, 6, 141–184, <https://doi.org/10.1002/2013MS000265>, 2014.
- 1194 Sellers, P. J.: Modeling the Exchanges of Energy, Water, and Carbon Between Continents and
1195 the Atmosphere, 275, 502–509, <https://doi.org/10.1126/science.275.5299.502>, 1997.
- 1196 Simard, M., Pinto, N., Fisher, J. B., and Baccini, A.: Mapping forest canopy height globally with
1197 spaceborne lidar, 116, <https://doi.org/10.1029/2011JG001708>, 2011.
- 1198 Singh, A. K., Dhanapal, S., and Yadav, B. S.: The dynamic responses of plant physiology and
1199 metabolism during environmental stress progression, *Mol Biol Rep*, 47, 1459–1470,
1200 <https://doi.org/10.1007/s11033-019-05198-4>, 2020.
- 1201 Sitch, S., Smith, B., Prentice, I. C., Arneth, A., Bondeau, A., Cramer, W., Kaplan, J. O., Levis,
1202 S., Lucht, W., Sykes, M. T., Thonicke, K., and Venevsky, S.: Evaluation of ecosystem dynamics,
1203 plant geography and terrestrial carbon cycling in the LPJ dynamic global vegetation model, 9,
1204 161–185, <https://doi.org/10.1046/j.1365-2486.2003.00569.x>, 2003.
- 1205 Sitch, S., Friedlingstein, P., Gruber, N., Jones, S. D., Murray-Tortarolo, G., Ahlström, A.,
1206 Doney, S. C., Graven, H., Heinze, C., Huntingford, C., Levis, S., Levy, P. E., Lomas, M.,
1207 Poulter, B., Viovy, N., Zaehle, S., Zeng, N., Arneth, A., Bonan, G., Bopp, L., Canadell, J. G.,
1208 Chevallier, F., Ciais, P., Ellis, R., Gloor, M., Peylin, P., Piao, S. L., Le Quéré, C., Smith, B., Zhu,



- 1209 Z., and Myneni, R.: Recent trends and drivers of regional sources and sinks of carbon dioxide,
1210 *Biogeosciences*, 12, 653–679, <https://doi.org/10.5194/bg-12-653-2015>, 2015.
- 1211 Strigul, N., Pristinski, D., Purves, D., Dushoff, J., and Pacala, S.: Scaling from trees to forests:
1212 tractable macroscopic equations for forest dynamics, 78, 523–545, [https://doi.org/10.1890/08-](https://doi.org/10.1890/08-0082.1)
1213 0082.1, 2008.
- 1214 Sulman, B. N., Shevliakova, E., Brzostek, E. R., Kivlin, S. N., Malyshev, S., Menge, D. N. L.,
1215 and Zhang, X.: Diverse Mycorrhizal Associations Enhance Terrestrial C Storage in a Global
1216 Model, 33, 501–523, <https://doi.org/10.1029/2018GB005973>, 2019.
- 1217 Swenson, N. G. and Enquist, B. J.: Ecological and evolutionary determinants of a key plant
1218 functional trait: wood density and its community-wide variation across latitude and elevation, 94,
1219 451–459, <https://doi.org/10.3732/ajb.94.3.451>, 2007.
- 1220 Tifafi, M., Guenet, B., and Hatté, C.: Large Differences in Global and Regional Total Soil
1221 Carbon Stock Estimates Based on SoilGrids, HWSD, and NCSCD: Intercomparison and
1222 Evaluation Based on Field Data From USA, England, Wales, and France, 32, 42–56,
1223 <https://doi.org/10.1002/2017GB005678>, 2018.
- 1224 Tilman, D.: Plant strategies and the dynamics and structure of plant communities, Princeton
1225 University Press, Princeton, N.J, 360 pp., 1988.
- 1226 Verryckt, L. T., Vicca, S., Van Langenhove, L., Stahl, C., Asensio, D., Urbina, I., Ogaya, R.,
1227 Llusà, J., Grau, O., Peguero, G., Gargallo-Garriga, A., Courtois, E. A., Margalef, O., Portillo-
1228 Estrada, M., Ciais, P., Obersteiner, M., Fuchslueger, L., Lugli, L. F., Fernandez-Garberí, P.-R.,
1229 Vallicrosa, H., Verlinden, M., Ranits, C., Vermeir, P., Coste, S., Verbruggen, E., Bréchet, L.,
1230 Sardans, J., Chave, J., Peñuelas, J., and Janssens, I. A.: Vertical profiles of leaf photosynthesis
1231 and leaf traits and soil nutrients in two tropical rainforests in French Guiana before and after a 3-
1232 year nitrogen and phosphorus addition experiment, 14, 5–18, [https://doi.org/10.5194/essd-14-5-](https://doi.org/10.5194/essd-14-5-1232)
1233 1232, 2022.
- 1234 Volaire, F.: A unified framework of plant adaptive strategies to drought: Crossing scales and
1235 disciplines, 24, 2929–2938, <https://doi.org/10.1111/gcb.14062>, 2018.
- 1236 Wang, H., Prentice, I. C., Keenan, T. F., Davis, T. W., Wright, I. J., Cornwell, W. K., Evans, B.
1237 J., and Peng, C.: Towards a universal model for carbon dioxide uptake by plants, 3, 734–741,
1238 <https://doi.org/10.1038/s41477-017-0006-8>, 2017.
- 1239 Wang, Y.-P. and Goll, D. S.: Modelling of land nutrient cycles: recent progress and future
1240 development, *Fac Rev*, 10, 53, <https://doi.org/10.12703/r/10-53>, 2021.
- 1241 Wang, Y.-P., Trudinger, C. M., and Enting, I. G.: A review of applications of model–data fusion
1242 to studies of terrestrial carbon fluxes at different scales, 149, 1829–1842,
1243 <https://doi.org/10.1016/j.agrformet.2009.07.009>, 2009.
- 1244 Weng, E. and Luo, Y.: Relative information contributions of model vs. data to short- and long-
1245 term forecasts of forest carbon dynamics, 21, 1490–1505, 2011.



- 1246 Weng, E., Luo, Y., Gao, C., and Oren, R.: Uncertainty analysis of forest carbon sink forecast
1247 with varying measurement errors: a data assimilation approach, 4, 178–191,
1248 <https://doi.org/10.1093/jpe/rtr018>, 2011.
- 1249 Weng, E., Fariior, C. E., Dybzinski, R., and Pacala, S. W.: Predicting vegetation type through
1250 physiological and environmental interactions with leaf traits: evergreen and deciduous forests in
1251 an earth system modeling framework, 23, 2482–2498, <https://doi.org/10.1111/gcb.13542>, 2017.
- 1252 Weng, E., Dybzinski, R., Fariior, C. E., and Pacala, S. W.: Competition alters predicted forest
1253 carbon cycle responses to nitrogen availability and elevated CO₂: simulations using an explicitly
1254 competitive, game-theoretic vegetation demographic model, 16, 4577–4599,
1255 <https://doi.org/10.5194/bg-16-4577-2019>, 2019.
- 1256 Weng, E. S., Malyshev, S., Lichstein, J. W., Fariior, C. E., Dybzinski, R., Zhang, T.,
1257 Shevliakova, E., and Pacala, S. W.: Scaling from individual trees to forests in an Earth system
1258 modeling framework using a mathematically tractable model of height-structured competition,
1259 12, 2655–2694, <https://doi.org/10.5194/bg-12-2655-2015>, 2015.
- 1260 Wieder, W. R., Grandy, A. S., Kallenbach, C. M., and Bonan, G. B.: Integrating microbial
1261 physiology and physio-chemical principles in soils with the Microbial-MIneral Carbon
1262 Stabilization (MIMICS) model, 11, 3899–3917, <https://doi.org/10.5194/bg-11-3899-2014>, 2014.
- 1263 Williams, M., Richardson, A. D., Reichstein, M., Stoy, P. C., Peylin, P., Verbeeck, H.,
1264 Carvalhais, N., Jung, M., Hollinger, D. Y., Kattge, J., Leuning, R., Luo, Y., Tomelleri, E.,
1265 Trudinger, C. M., and Wang, Y.-P.: Improving land surface models with FLUXNET data,
1266 *Biogeosciences*, 6, 1341–1359, <https://doi.org/10.5194/bg-6-1341-2009>, 2009.
- 1267 Woodward, F. I., Lomas, M. R., and Betts, R. A.: Vegetation-climate feedbacks in a greenhouse
1268 world, *Phil. Trans. R. Soc. Lond. B*, 353, 29–39, <https://doi.org/10.1098/rstb.1998.0188>, 1998.
- 1269 Xu, T., White, L., Hui, D., and Luo, Y.: Probabilistic inversion of a terrestrial ecosystem model:
1270 Analysis of uncertainty in parameter estimation and model prediction, 20, GB2007,
1271 <https://doi.org/10.1029/2005GB002468>, 2006.
- 1272 Yuan, W., Luo, Y., Liang, S., Yu, G., Niu, S., Stoy, P., Chen, J., Desai, A. R., Lindroth, A.,
1273 Gough, C. M., Ceulemans, R., Arain, A., Bernhofer, C., Cook, B., Cook, D. R., Dragoni, D.,
1274 Gielen, B., Janssens, I. A., Longdoz, B., Liu, H., Lund, M., Matteucci, G., Moors, E., Scott, R.
1275 L., Seufert, G., and Varner, R.: Thermal adaptation of net ecosystem exchange, 8, 1453–1463,
1276 <https://doi.org/10.5194/bg-8-1453-2011>, 2011.
- 1277 Zeng, Z., Piao, S., Li, L. Z. X., Zhou, L., Ciais, P., Wang, T., Li, Y., Lian, X., Wood, E. F.,
1278 Friedlingstein, P., Mao, J., Estes, L. D., Myneni, R. B., Peng, S., Shi, X., Seneviratne, S. I., and
1279 Wang, Y.: Climate mitigation from vegetation biophysical feedbacks during the past three
1280 decades, 7, 432–436, <https://doi.org/10.1038/nclimate3299>, 2017.
- 1281 Zhou, G., Houlton, B. Z., Wang, W., Huang, W., Xiao, Y., Zhang, Q., Liu, S., Cao, M., Wang,
1282 X., Wang, S., Zhang, Y., Yan, J., Liu, J., Tang, X., and Zhang, D.: Substantial reorganization of



- 1283 China's tropical and subtropical forests: based on the permanent plots, 20, 240–250,
1284 <https://doi.org/10.1111/gcb.12385>, 2014.
- 1285 Zuleta, D., Arellano, G., Muller-Landau, H. C., McMahon, S. M., Aguilar, S., Bunyavejchewin,
1286 S., Cárdenas, D., Chang-Yang, C.-H., Duque, A., Mitre, D., Nasardin, M., Pérez, R., Sun, I.-F.,
1287 Yao, T. L., and Davies, S. J.: Individual tree damage dominates mortality risk factors across six
1288 tropical forests, 233, 705–721, <https://doi.org/10.1111/nph.17832>, 2022.
- 1289